FEASIBILITY STUDY ON THE IMPLEMENTATION OF PLANAR INDUCTORS ONTO C-SI SOLAR CELLS THROUGH NUMERICAL SIMULATIONS

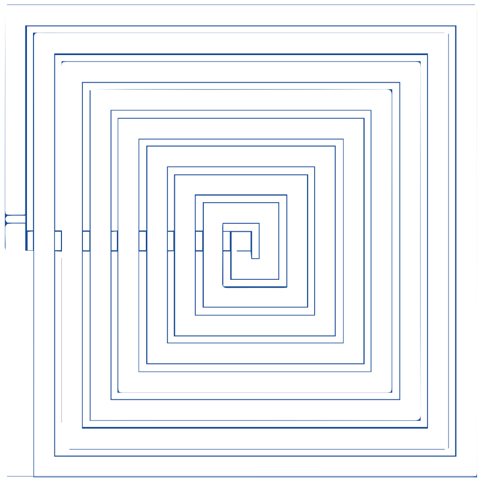

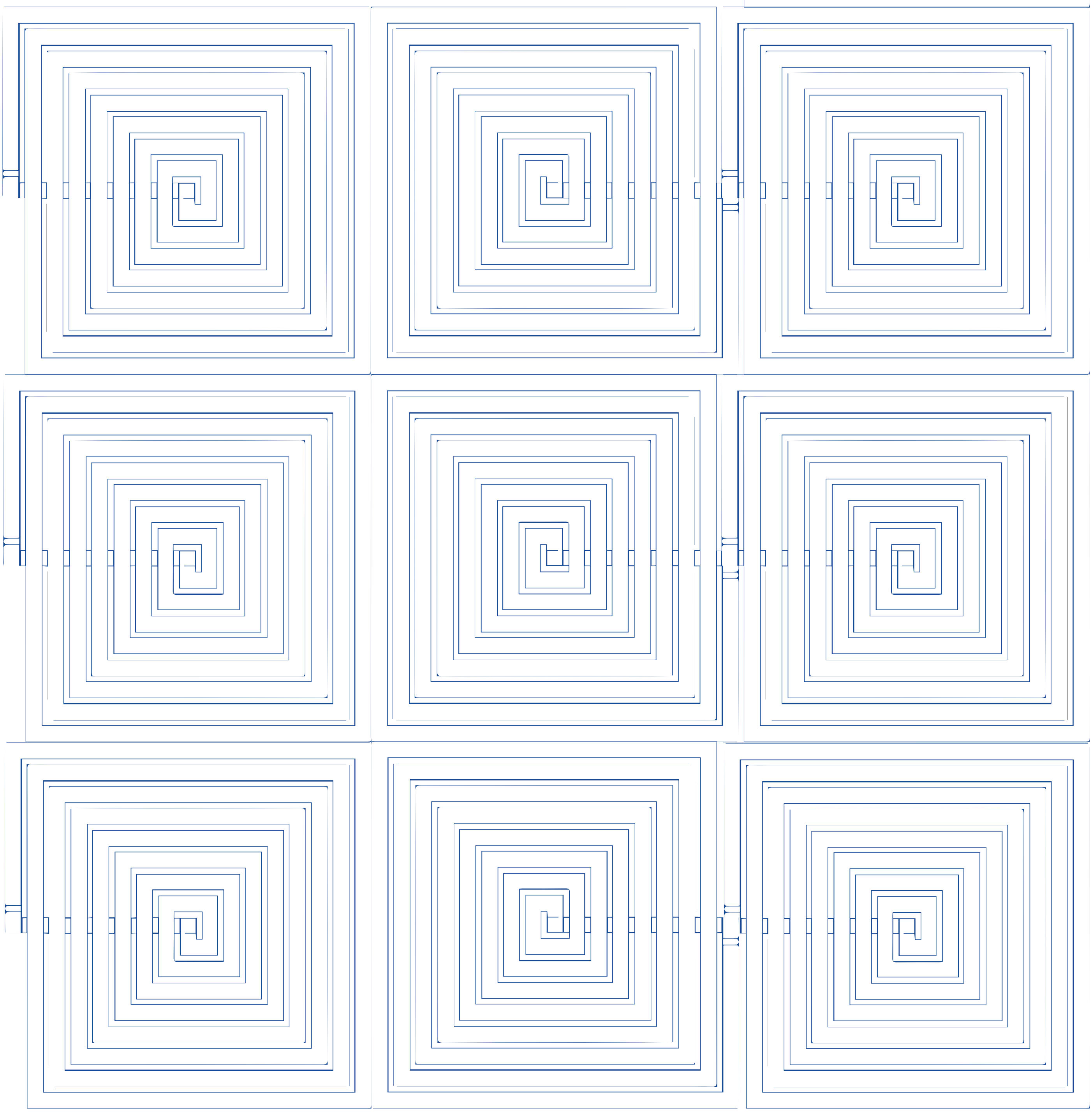

Delft University of Technology

MSc. Thesis Report | Jim Voorn

Feasibility study on the implementation of planar inductors onto c-Si solar cells through numerical simulations

by

Jim Voorn

to obtain the degree of Master of Science
at the Delft University of Technology,
to be defended publicly on Wednesday July 13, 2022 at 10:00 AM.

Student number:	4379268	
Project duration:	December 1, 2021 – July 13, 2022	
Thesis committee:	Prof. dr. A.W. Weeber	TU Delft, Professor
	Dr. P. Manganiello,	TU Delft, Assistant Professor & Supervisor
	Dr. G.R. Chandra Mouli	TU Delft, Assistant Professor
	Ir. D.A. van Nijen,	TU Delft, PhD candidate & Daily supervisor

This thesis is confidential and cannot be made public until July 13, 2024.

Preface

Before you lies my master thesis project titled 'Feasibility study on the implementation of planar inductors onto c-Si solar cells through numerical simulations', which I carried out in partial fulfillment of the master's program for Sustainable Energy Technology (SET) at the Delft University of Technology. After finishing the bachelor Applied Physics, a more sustainable direction appealed to me, after which I have chosen SET with a specific direction in *Solar, Power,* and *Economics*. During my master's, I have gained a lot of insight and knowledge on different energy systems, and I believe that solar energy will play a major role in the energy transition.

The aim of this thesis project was to design and simulate a square planar inductor for the integration onto a c-Si solar cell. Though the initial idea of the project was to not only simulate but also create a planar inductor, unfortunately, due to a limited amount of time, this has not been achieved. I do want to state, however, that I have greatly enjoyed this thesis and have learned a lot about power electronics and modeling in COMSOL.

I would like to express my gratitude to my daily supervisor, David van Nijen, for making the time to meet with me twice a week and always being available on short notice. He has taught me a lot and really given me an insight into how to construct and approach a thesis project. Secondly, I would like to thank Dr. Patrizio Manganiello for the energy and enthusiasm during the entire project and for sharing his knowledge during the monthly meetings where there was always room for questions and debate. I also want to thank everyone from the PVMD group who has helped me during my thesis. Lastly, I want to thank Katarina and Yavuzhan for helping each other through the past 7 months and keeping the office a serious but fun place to be. In addition, I would like to thank Prof. Arthur Weeber and Dr. Chandra Mouli for being part of my graduation committee.

Finally, I would like to thank my girlfriend, my friends, and my family for their support and for guiding me when necessary throughout my thesis.

Jim Voorn
Delft, July 2022

Abstract

With the integration of solar panels in urban areas, where shading is a common issue, it is desired to realize more shade-resilient designs. A DC-DC boost converter is an electronic device that can be used for maximum power point tracking (MPPT). When implementing MPPT at sub-module level, the shade resilience of the module can be increased. This thesis aims to investigate the feasibility of implementing planar inductors into c-Si solar cells using the numerical simulation software COMSOL Multiphysics®.

Through simulations, the inductance and resistance values for various planar coil geometries were obtained. Subsequently, the feasibility of using these coils in a sub-module DC-DC boost converter was investigated. For this study, a specific case was assumed where a *Gen 2 Cell - 160 mm* c-Si cell is used with a DC-DC boost converter with a duty cycle of 0.5 and a current ripple of 20%. Given the parameters from these devices, the minimum required inductance of 1.20 μH for a frequency of 200 kHz and 2.40 μH for a frequency of 100 kHz were obtained. The series resistances that can be added to the solar cell while still maintaining high efficiency, range from 1.0 $m\Omega$ to 4.8 $m\Omega$, for a 1% to a 5% power loss, respectively. This is all for single-cell power conversion.

Two different approaches have been examined; the *screen-printed coil(s)* approach and the *screen printing thickness exceeding coil(s)* approach. The former studies coils that do not exceed the maximum thickness achievable with screen printing. As such, these coils could be simpler to implement into a solar cell production line than coils with a higher thickness. In this research, for thicknesses below 300 μm a best-case scenario is studied where the skin effect is neglected. The latter studies a larger range of thicknesses, not taking any specific production method into account, but the skin and proximity effect is taken into account. *The screen-printed* approach is limited to a thickness range of 10 μm to 200 μm, thus simulated by the 2D model. For the air-core single-cell inductors for DC-DC boost converter applications, the inductance and resistance values were either below the 1.20 μH threshold or above the 4.8 $m\Omega$ threshold, respectively. These thresholds change depending on the number of series-connected cells. The inductance of a planar inductor can be boosted up to 200% when adding a magnetic material in a sandwich structure, however, this will also increase the costs of the application. In a boosted-inductance case, the 3-turn coil with a thickness of 200 μm, and a 5% power loss is the only configuration that is feasible for a 200 kHz DC-DC boost converter application, with an inductance of 1.569 μH and a resistance of 3.45 $m\Omega$. By increasing the number of coils per cell, the power dissipation in the coils can be reduced. Using this approach, six feasible topologies can be created. One of those is the nine parallel-connected 8-turn coils with a thickness of 200 μm, reaching an inductance of 1.210 μH and a resistance of 3.186 $m\Omega$, allowing for a 200 kHz DC-DC boost converter application without any magnetic inductance increase. All six options are feasible for integration on a single cell using screen printing, however, the actual resistances will be higher due to the skin and proximity effect, and single-cell integration will be too expensive for industrial applications. When studying thicknesses above the screen printing limit, only the 4-turn coil with a thickness of 300 μm, a magnetically increased inductance of 2.718 μH, and a resistance of 4.01 $m\Omega$, is feasible for the 100 and 200 kHz frequencies. This case however does neglect the skin effect. For the 3D model and thicknesses above 400 μm, the skin effect significantly impacts the resistance. When series connecting multiple cells to a single coil, the only feasible option is the eight-cell connected 8-turn coil for a thickness of 200 μm and 300 μm, both reaching a magnetically increased inductance of 10.431 μH and resistance of 23.33 $m\Omega$ and 15.56 $m\Omega$, respectively.

Contents

List of Figures

List of Tables

Nomenclature

Abbreviations

Abbreviation	Definition
AC	Alternating Current
CCM	Continuous Conduction Mode
DC	Direct Current
DCM	Discontinuous Conduction Mode
EMF	Electromotive Force
FEM	Finite Element Method
HF	High Frequency
IED	Infinite Element Domain
MPP	Maximum Power Point
MPPT	Maximum Power Point Tracking
PDE	Partial Differential Equation
PWM	Pulse-Width-Modulation
STC	Standard Test Conditions
WPT	Wireless Power Transfer

1
Introduction

This chapter provides some background on the relevance of this thesis, and describes the project in detail. Several of the theory mentioned in this chapter will be further explained in Chapter 2 *Theoretical background*

1.1. Human influence on the environment

Greenhouse gasses are essential to life on Earth, trapping heat from the Sun in the atmosphere, resulting in a livable temperature. As can be seen in Figure 1.1, the greenhouse gas concentration on Earth has been fluctuating over the past hundreds of thousands of years, resulting in both warmer (*interglacial*) and colder (*glacial*) periods. Since the start of the Industrial Revolution in 1750, the CO_2 concentration has been rising at a historically high pace. The last time the atmospheric CO_2 levels were this high was over 3 million years ago, with temperatures 2°- 3°C higher than pre-industrial times, and sea levels 15-25 meters higher than today [1].

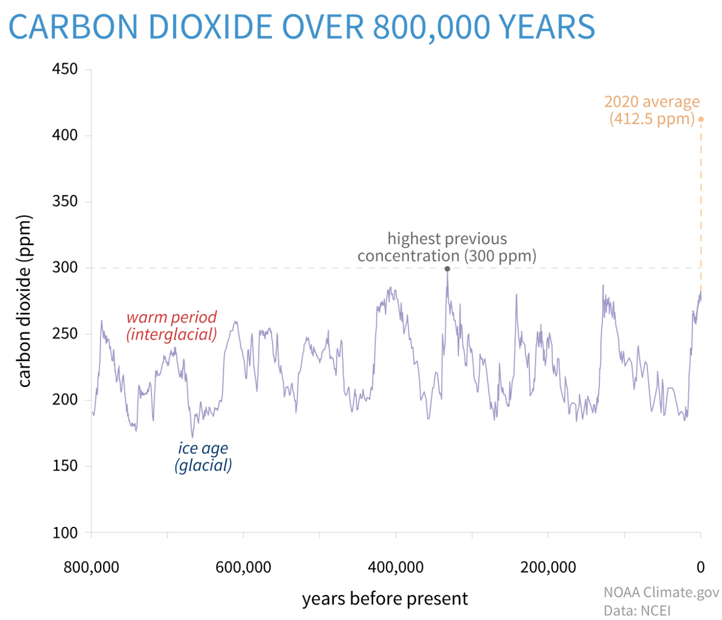

Figure 1.1: Carbon dioxide concentration over the past 800,000 years [1].

Since the 1980s, each decade has been warmer than the previous one, according to the World Meteorological Organization, and 2021 is one of the seven warmest years on record, with an average of 1.11 (± 0.13) °C above pre-industrial era levels [2]. Carbon dioxide levels are mostly rising because of the burning of fossil fuels, which contain carbon pulled out of the atmosphere through photosynthesis by plants over many millions of years. With our energy mainly coming from fossil fuels, like coal, oil, and gas, we currently emit around 50 billion tonnes of CO_2e each year, which is more than 40% higher than the emissions in 1990 [3]. The largest single source of greenhouse gas emissions is the electricity and heat production sector, which contributes to 25% of the total amount of global emissions in 2010 [4]. With more economic sectors electrifying, it is expected that this number will only increase if we keep producing electricity by burning fossil fuels. For that reason, we must look for more sustainable ways of producing energy.

1.2. Solar energy

One such sustainable energy source is solar energy. With The Sun being the largest energy source at our disposal, carrying sun rays to the planet Earth with an immense amount of energy, it delivers around 89,300 TWh of energy every hour [5]. Photovoltaic (PV) solar systems transform the energy of sunlight into electricity using solar cells. Photovoltaic systems have become one of the leading technologies among the sustainable energy sources, reaching a total gross electricity production of 821 TWh globally in 2020, accounting for 3.1% of the global energy generation. This makes it the third-largest renewable energy source behind hydropower and onshore wind [6]. The installed global power capacity from solar energy has increased exponentially from 0.65 GW in 2000 to 707.50 GW in 2020, see Figure 1.2. However, the PV market is still rather small in comparison to well-established conventional energy sources, such as coal.

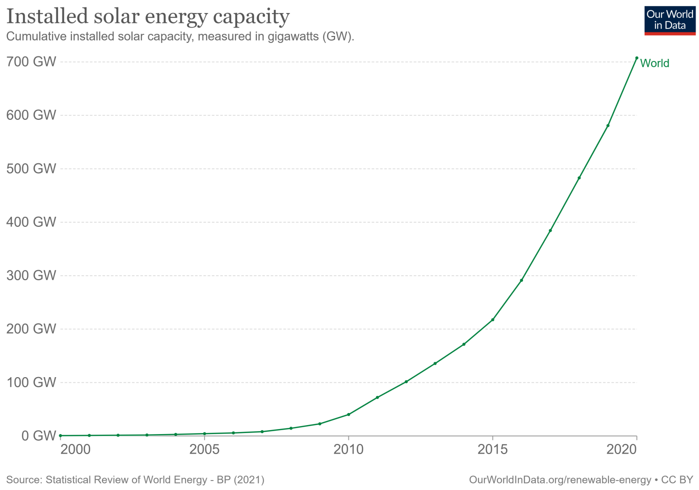

Figure 1.2: Installed solar PV capacity from 2000 to 2020 worldwide [7]

Part of this growth is due to the decrease in the Levelized Cost of Electricity (LCOE) of PV modules over the past decade [8]. Decreasing solar PV module prices, Balance of System (BoS) costs, and an increasing capacity factor, have already led to solar electricity costs through power purchase agreements below US$0.02/kWh in sunny countries and US$0.047/kWh in Germany [9]. Around 95% of this capacity is based on crystalline silicon (c-Si) solar cells [10].

There are two main types of configurations for solar cells; the front-back contacted (FBC) and interdigitated back contacted (IBC) solar cell, as presented in Figure 1.3. The FBC has the metal contacts for charge carrier collection on both sides of the wafer, as is most common for the commercial c-Si solar cells used today. The newer IBC structure has all the contacts located on the back of the cell, eliminating the shading losses that take place with the FBC structure. The metal finger pattern on the front side of an FBC cell is already highly optimized for minimal shading and resistive losses, but there might be room to create spiral-like patterns on the backside since no shading losses are taking place there [11].

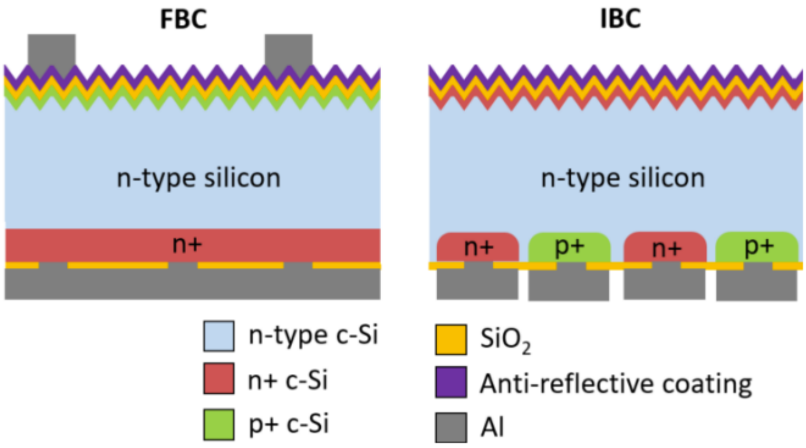

Figure 1.3: The front-back contacted (FBC) solar cell is shown on the left, with the metal contacts on both sides of the wafer, and the interdigitated back contacted (IBC) solar cell is shown on the right, with the metal contacts on the backside of the wafer [12].

1.3. Power electronics

Though there are different types of PV systems, like stand-alone, grid-connected, or hybrid systems, they all need power electronics to operate properly. Some of the electronics are DC-DC converters, inverters, and charge controllers. They are used for Maximum Power Point Tracking (MPPT), conversion from DC to DC and DC to AC power, and to control the charge that is flowing to and from the battery system, if there is one present in the system. The configuration of the different PV systems does differ from one another. In grid-connected systems, the inverter is directly connected from the PV array to the grid and converts the DC electricity from the PV array into AC electricity needed by the grid. Sometimes the inverter also contains a DC-DC converter, to convert the variable panel voltage into a constant voltage used by the inverter. In stand-alone systems, the inverter is usually connected to a charge controller and the battery system. As the solar system needs to generate the absolute maximum amount of energy to the load or the grid, the inverters should be highly efficient. A distinguishment can be made between *single-phase* and *three-phase* inverters, where the first is mainly used for low-power PV systems, and the latter for higher-power PV systems. In Figure 1.4, a set of four different topologies of inverters can be seen. These are not all the topologies, but the most widely used ones in practice [13].

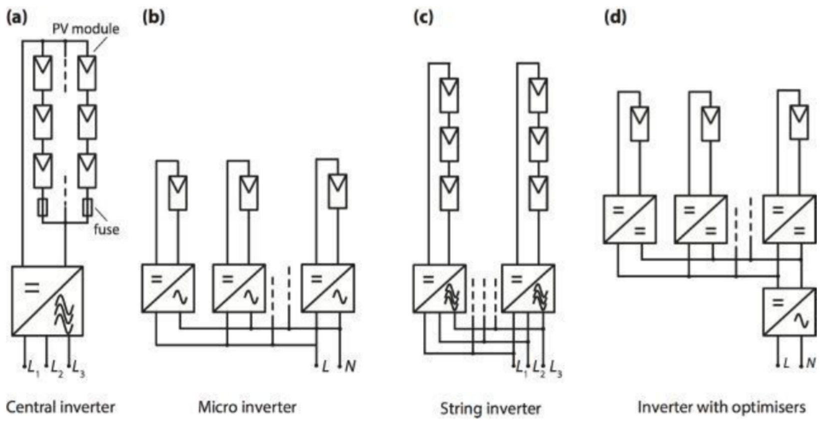

Figure 1.4: Different inverter topologies [13]

The four topologies are the central inverter, micro-inverter, string inverter, and inverter with optimizers. The central inverter has the simplest architecture as seen in Figure 1.4 (a), where series-connected

PV modules are connected in parallel creating a PV array, which in turn is connected to the inverter. Due to its low specific cost and few components, the central inverter is a very reliable topology and is mostly used for large-scale PV power plants. Here also arises the disadvantage of the central inverter being less flexible and having high losses during current mismatching between different PV modules.

The micro inverter is presented in Figure 1.4 (b), where each inverter is directly connected to one or several PV modules. This allows for module optimal MPPT and minimizes the mismatch losses from non-optimal MPPT, present in the central inverter. The inverter first boosts the DC voltage to the required value, since the PV module has a low voltage rating. Then the voltage is converted from DC to AC, allowing for grid connection or AC loads. These micro-inverters are closely placed to the PV panels, sometimes even directly integrated into the panels (*AC PV panels*) [13]. This wide range of advantages does come at a certain cost. Due to their placement, the environment of the inverters is the same as that of a PV module. These environments are all but generous for inverters, with strongly varying temperatures and high-temperature peaks [14]. The micro inverter has the highest specific cost of the four inverter topologies and the inverter efficiency is also lower, due to the low PV module voltage which has to be boosted a lot to reach the desired AC voltage.

For smaller PV systems, like households or office buildings, the string inverter (Figure 1.4 (c)) is used, where there is more need for accurate MPPT. It combines the advantages of both the central and micro-inverters, with a high power-rating and more controllable MPPT. One disadvantage is that due to the high open-circuit voltages (up to 1 kV), the protection of the system requires extra consideration, especially since string inverters are mainly installed in households or offices [13].

Lastly, there is the inverter with optimizers topology, shown in Figure 1.4 (d), which is a combination of a central inverter with module-level power optimizers, where every module can operate at its oPP. This is possible since every optimizer contains both an MPP tracker and DC-DC converter, allowing a wider range of input voltages for the system to operate without losing power.

One of the big issues that can occur at both the central and string inverter, is the formation of hotspots. This generally occurs when (partial) shading takes place or the cell is damaged or connected incorrectly. Hotspot heating can occur when a large number of series-connected cells cause a reverse bias across the shaded cell, leading to the dissipation of power in the shaded or faulty cell. All the generating capacity of the good cells is dissipated as heat in the faulty cell. When this enormous power dissipation occurs in a small area in the faulty cell, it can lead to local overheating, or 'hot-spots', which in turn can lead to destructive effects [15].

With the increase of urban PV applications, partial shading of solar cells is becoming more and more present. There are several ways to overcome the problems that arise when (partial) shading takes place. Apart from the micro inverter, another solution is the integration of a bypass diode. Modern PV modules often contain 60 or 72 solar cells and are usually connected in series. In a series connection, however, the overall current is limited by the lowest current-producing cell, as opposed to a parallel connection where the overall current is the sum of all parallel-connected current-producing cells. By connecting a bypass diode parallel to a set of series-connected cells, the string of cells is bypassed in case of a mismatch. If no mismatch takes place, the bypass diode will be in the off-state and blocks the flow of current, allowing the current to flow through the string of solar cells. If a mismatch does occur, due to for instance shading, the bypass diode will be in the on-state, allowing the current to flow through the bypass diode and not through the string of solar cells. By increasing the number of bypass diodes, the effects of current mismatching can be reduced. This does come at the cost of increased losses from the diode, since there is a (slight) voltage drop when the diode is active, but also leakage currents will be present when the diode is inactive. An example of a typical industrial module with 60 cells and three bypass diodes can be seen if Figure 1.5.

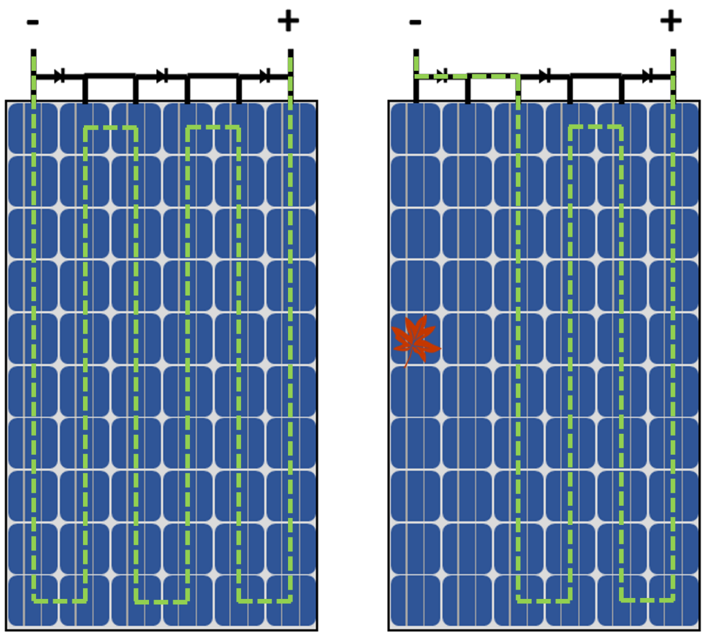

Figure 1.5: The left figure shows the current flow when no shading takes place, whereas the right figure shows a panel with shading, eliminating a string of cells.

1.4. Cell-integrated electronics

To extend the different PV applications and maximize the harvest of the available solar energy, the next generation of intelligent PV-based devices has to be developed. These PV devices will not only generate electricity but include many functionalities. The research field that focuses on this combination of intelligent PV and digital technologies is called photovoltatronics, which aims at maximizing the generation of electricity and its utilization. To continuously deliver optimal useful energy from PV generators, they have to be equipped with intelligence that can adapt to the changing conditions of operation. One way of adding intelligence is by integrating electronics and sensors onto a PV cell [16]. The integration of power electronics could lead to a more controlled MPPT of a set of PV cells, or even a single cell, which in turn could reduce for instance the losses from shading, thus creating shade-resilient solar panels.

1.5. Equivalent models

1.5.1. Solar cell

The operation of a PV cell can be described using an equivalent circuit model, as can be seen in Figure 1.6. An ideal current source delivers current proportional to the photocurrent that is generated in the cell. Two conditions are of interest for the equivalent circuit, which is the short-circuit current (I_{sc}) and the open-circuit voltage (V_{oc}). These two conditions are further explained in Section 2.3. In Figure 1.6 a PV equivalent circuit with resistive elements, that would account for power losses, is shown. The resistive elements are made up of a parallel shunt resistance R_{sh} and a series resistance R_s. The former is mainly due to manufacturing defects, resulting in a low shunt resistance which causes losses in the solar cell by providing an alternate current path for the current generated by the light [17, 18]. The series resistance is mainly formed due to three causes: the movement of current through the solar cell, the resistance between the metal contact and the silicon, and the resistance due to the connection to the metal contacts [19, 20].

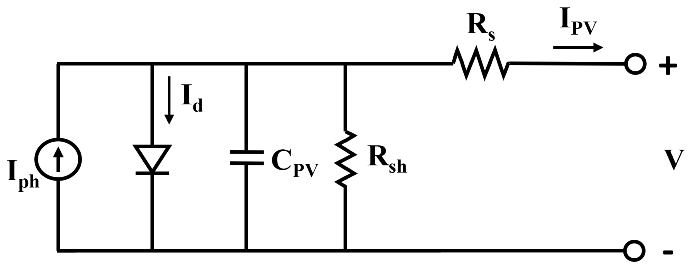

Figure 1.6: Equivalent model of a PV cell

1.5.2. DC-DC boost converter

Since the output voltage of the PV modules is not always constant, a DC-DC converter can be placed between the PV module and the inverter, transforming the variable module voltage into a constant voltage. It is a medium of power transmission to perform energy absorption and injection from a solar panel to a grid-tied inverter. Furthermore, a DC-DC converter can be used to perform maximum power point tracking (MPPT), which controls the operating point of the modules. The energy absorption and injection are performed by a combination of four components, which are the inductor, the transistor, the diode, and the capacitor. Two important topologies of DC-DC converters are the *buck* (or Step-down), and the *boost* (or Step-up) [21]. A circuit model of a DC-DC boost converter can be seen in Figure 1.7, where the inductor is the first component in the model. When connecting a PV module to a boost converter, the inductor will be series connected to the PV module, allowing for a shift in the placement of the inductor to the module.

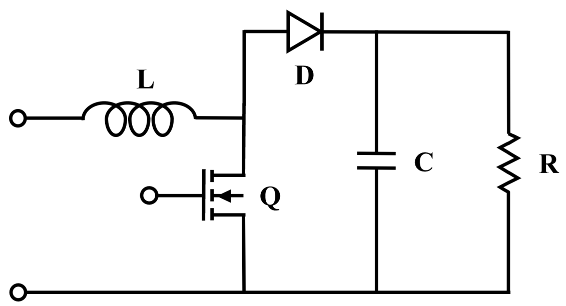

Figure 1.7: Circuit of a DC-DC boost converter

1.5.3. Combined circuit models

Most of the time the PV power electronics are housed in the junction box, which is situated on the back side of the solar panel. Integrating parts of the power electronic components into the design of a c-Si solar cell opens up new ways of designing PV modules. Most DC-DC boost converters are placed in the junction box, where the inductor is most of the time the most expensive and bulky component [22]. Inductors are one of the basic components of power electronics relevant to PV modules. It is usually a coil of wire that sets up an alternating magnetic field when an alternating current passes through it, and the inductance is the property of an inductor that opposes the change in current. It would be beneficial to create solar cells with a high self-inductance to replace the inductor from the DC-DC boost converter. One way of measuring the performance of an inductor is by studying the quality factor, which is a measure of inductance over resistance for a given frequency. There is however a trade-off for finding the highest quality factor, as most of the time with an increasing number of turns, the inductance increases, but so will the resistance. This trade-off will be further discussed in this research.

When examining the equivalent model of both the PV cell and the DC-DC boost converter, there is a possibility to create smaller, simpler, and cheaper designs [12]. When connecting a DC-DC boost converter to a solar cell, the inductor will be series connected to the series resistance. A new proposed model will be discussed in this report, which can be seen in Figure 1.8, where the blue dotted part indicates the PV sub-module with increased self-inductance, and the green dotted part indicates the new boost converter without an inductor. In this research, it is assumed that the PV capacitor has a high enough capacitance to create a low voltage ripple.

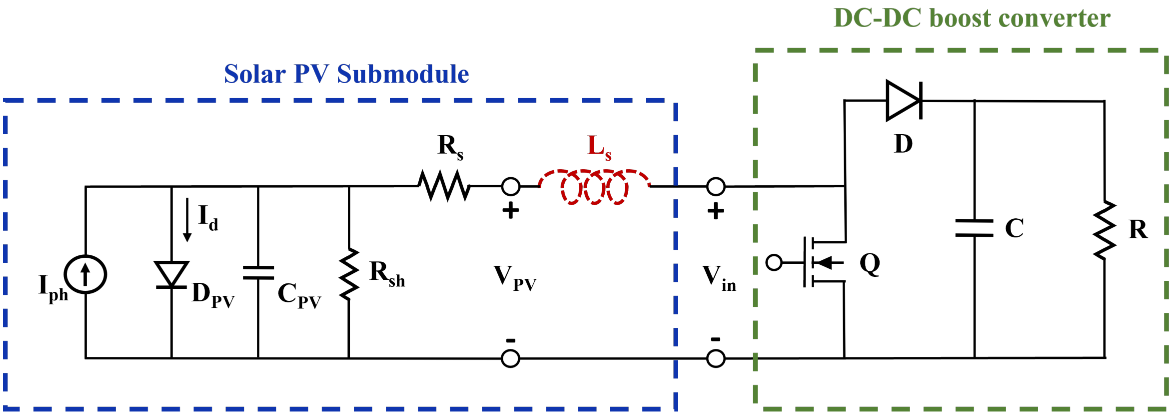

Figure 1.8: The new proposed model, where the inductor (red) is shifted from the DC-DC boost converter to the PV cell, increasing the self-inductance of the PV cell.

1.6. Project description and outline

This thesis project aims to research the possibility of integrating a planar inductor on the back side of a c-Si solar cell, where the main question is:

What is the feasibility of implementing a square planar inductor onto the backside of a c-Si solar cell for application in a DC-DC boost converter?

To answer this question, a multitude of sub-questions have been formulated:

1. What is the required inductance for DC-DC boost converter applications in PV modules?
2. What is the maximum allowed series resistance caused by adding a square planar inductor to a c-Si solar cell?
3. What inductance and resistance values can be achieved by implementing a square planar inductor into the fabrication process of a c-Si solar cell?
4. How does the performance of a square planar inductor depend on the number of turns and conductor thickness for varying frequencies?
5. How is a rectangular cross-sectional wire with varying dimensions affected by skin effect?

With the introduction to the subject given, the chapters are ordered as follows. The theoretical basics of PV technology, power electronics, (planar) inductors, and their integration onto PV cells will be discussed in Chapter 2. In Chapter 3 the different ways of achieving planar inductor integration are discussed, after which in Chapter 4 the created model is shown. Chapter 5 and Chapter 6 show the *screen printed coil(s)* method and the *screen printing thickness exceeding coil(s)* method, respectively. Lastly, the conclusions of this thesis work are presented in Chapter 7.

2
Theoretical background

This chapter covers some theoretical background of photovoltaic solar technology, inductors, and power electronics that are relevant for this thesis project.

2.1. Solar radiation

For the coming five billion years the Sun is a constant form of energy that emits enough sunlight on the Earth to handle the world's entire energy consumption for a year [23, 24]. With nuclear fusion taking place inside the Sun, we can approximate the surface, where the emission takes place, as a black body at a temperature of around 5800 K. The electromagnetic radiation that radiates from the Sun reaches the Earth in approximately 8 minutes in packets called *photons* of varying wavelengths [25]. These photons contain energy which is determined by their wavelength λ, and can be calculated with the following formula:

$$E_{ph} = \frac{hc}{\lambda} \tag{2.1}$$

Where c is the speed of light and h the Planck's constant.

Over $1.7 \cdot 10^{18}$ W of energy reaches the outer atmosphere of the Earth, in the so-called AM0 spectrum, where the irradiance is 1,361 W/m^2. Since parts of the light are scattered and absorbed in the Earth's atmosphere, and not everywhere on Earth the surface irradiance is equal, it is of utmost importance that there is a uniform way of comparing all the different solar cells and PV modules. These conditions are called the *standard test conditions* (STC), characterized by an irradiance of 1,000 W/m^2, a cell temperature of 25°C, and an AM1.5 spectrum. This AM1.5 spectrum is a reference to the solar irradiance on the Sun-facing plane on a surface tilt of 37°to the horizontal, corresponding to the 1,000 W/m^2 stated earlier. The spectral irradiances of a 6,000 K black body, the AM0 spectrum, and the AM1.5 spectrum are shown in Figure 2.1.

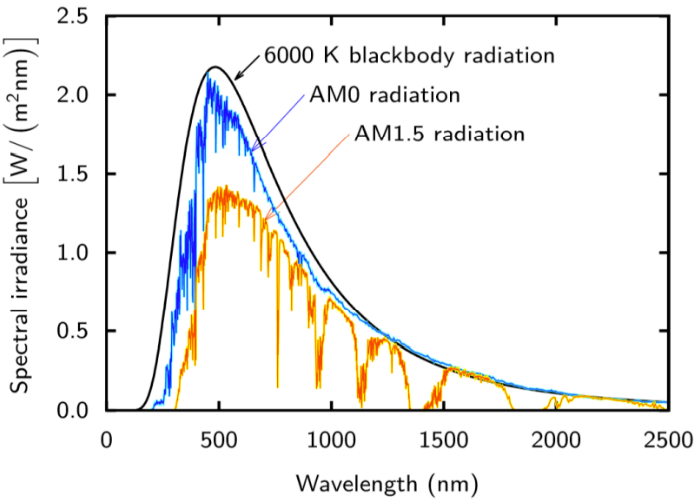

Figure 2.1: Spectral irradiance at different solar spectra [13].

2.2. Photovoltaic Fundamentals

The working principle of a solar cell is based on a potential difference at the junction of two different materials (p- and n-type materials) due to electromagnetic radiation (i.e. sunlight), also known as the *photovoltaic effect*. Charge carriers are created when an electron is excited from the valence band to the conduction band. The incoming light, with energy $E = hv$, excites an electron from the valence band to the conduction band, leaving behind a hole. When an electron is excited, it creates both a free electron in the conduction band and a free hole in the valance band. These are called *free charge carriers*. This happens in semiconductor materials when the photon energy is higher than the band gap energy. The electric field created in the p-n junction allows for the electrons and holes to flow in opposite directions, to the n-type and p-type doped layers, respectively. The charge carriers are then extracted at the electrical contacts and can be used to power an external circuit [20].

In practice, there are two main types of solar cells used: crystalline silicon (c-Si), and thin-film solar cells. Both types are suitable for the integration of a planar inductor, however, for this research, the focus will be only on c-Si solar cells, since they have the largest market share [26].

2.3. Solar cell parameters

In the following section, the main parameters that are used to quantify the results of a solar cell are explained.

2.3.1. Short circuit current

The *short circuit current* I_{sc} of a solar cell is the current that flows through the external circuit when the electrodes of the solar cell are short-circuited. The short circuit current is standardized to the AM1.5 spectrum since it is dependent on the photon flux incident on the cell. The short circuit current is dependent on the area of the solar cell. To remove the dependency on the area, the *short circuit current density* J_{sc} is often used to describe the maximum current delivered by a solar cell. Under the AM1.5 spectrum, the maximum possible current density for c-Si solar cells is 46 mA/cm^2, with commercial cells having a short circuit current density ranging from 28 mA/cm^2 to 40 mA/cm^2 [13, 27, 28].

2.3.2. Open circuit voltage

The *open-circuit voltage* V_{oc} is the voltage when the net current through the external circuit is zero and is the maximum voltage that a solar cell can deliver. It corresponds to the amount of forward bias in the solar cell, at which the diode current density compensates for the photocurrent density. The open-circuit voltage can be calculated with the following equation:

$$V_{oc} = \frac{k_B T}{q} ln\left(\frac{J_{ph}}{J_0} + 1\right) \approx \frac{k_B T}{q} ln\left(\frac{J_{ph}}{J_0}\right) \tag{2.2}$$

In Equation (2.2), k_B is the Boltzmann constant, T the temperature, and q the elementary charge constant, where the approximation is made when $J_{ph} \gg J_0$. The equation shows that the open-circuit voltage is dependent on the photocurrent density J_{ph} and the dark current density (also known as the saturation current density) J_0. The photocurrent density is the current resulting from the flux of photogenerated carriers, and the dark current density depends on the recombination in the solar cell. For this reason, the V_{oc} is seen as a measure of the amount of recombination. Under AM1.5 conditions, c-Si solar cells in the laboratory have reached a V_{oc} of 754 mV [29], while most commercial solar cells typically have a V_{oc} around 690 mV[30].

2.4. Inductor

An inductor is a passive two-terminal electrical component that stores energy in the form of a magnetic field and typically consists of a conductor wound into a coil. It plays a critical role in power systems, filtering, and isolation. An inductor generates a magnetic field when a current passes through it or generates an electrical current in the presence of a changing magnetic field. In the case of a changing current, the time-varying magnetic field induces an *electromotive force* (emf) in the conductor. This induced voltage has, according to Lenz's law, a polarity opposing the change in current by which it is created. This means that if for instance the current through an inductor increases, the induced voltage will be negative at the end of the inductor and positive at the beginning of the inductor, tending to oppose the increase in current. When a direct current (DC) is applied to the inductor, it acts like a piece of wire which can conduct electricity. When an alternating current (AC) is applied to the inductor, it will oppose the change in current and convert the electrical current into a magnetic field. The two main categories under which a fixed inductor is classified are ferrite core inductors and air-core inductors. For the ferrite core inductor, the conductor is wound around a ferromagnetic core, as can be seen in Figure 2.2. The core is not electrically connected to the inductor and increases the magnetic field lines, thus increasing the inductance of the inductor. The air core inductor does not have a ferromagnetic core, but an air core instead. The advantage of an air-core over a ferrite core inductor is that no core and energy losses take place at high frequencies.

Figure 2.2: Three different inductors, where each wire is wound around a certain type of core [31].

Microchips, also known as integrated circuits (ICs), are a collection of both active (e.g. transistors) and passive (e.g. inductors) components formed on a single crystal semiconductor substrate which are connected by a metallization pattern. Since the area of the ICs is very small, ranging from a few square millimeters to around 600 mm^2, there is little room for a bulky inductor [32]. This is where the planar spiral inductor is integrated, as can be seen in Figure 2.3, also known as *thin-film inductors*. With the increased speed of silicon devices, IC inductors have increased in popularity for silicon-based radio frequency (*rf*) and high-frequency applications [33]. Though the topology of the planar inductor differs from that of the normal inductor shown in Figure 2.2, the working principles are the same. It has been experimentally demonstrated that thin-film inductors can be used for DC-DC power conversion, even though they yield a smaller inductance than a conventional inductor [34]. Most thin-film inductors are made of copper and they can be fabricated in different shapes spiral shapes, like circular, hexagonal, or square.

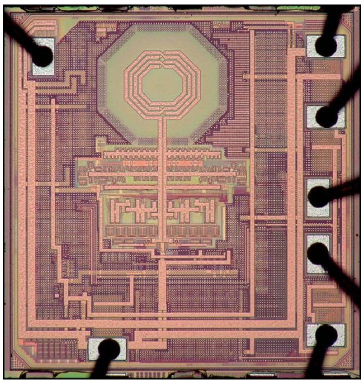

Figure 2.3: Planar inductor (hexagonal spiral on the top) on an integrated circuit (IC) [35].

An inductor is characterized by its inductance, which is measured in Henry (H), which usually has a quadratic dependency to the number of turns [36]. The inductance is the ratio of voltage to the rate of change of current. The inductance of a square coil as derived in [37] is given in Equation (2.3):

$$L_{square} = \frac{1.27\mu_0 N^2 d_{avg}}{2}\left(\ln\left(\frac{2.07}{\Delta}\right) + 0.18\Delta + 0.13\Delta^2\right) \tag{2.3}$$

Where μ_0 is the absolute magnetic permeability, N the number of turns, $d_{avg} = (d_{outer} + d_{inner})/2$ the average diameter of the coil, and $\Delta = (d_{outer} - d_{inner})/(d_{outer} + d_{inner})$ the fill ratio.

Under a sinusoidal steady-state condition, the current of an inductor lags the voltage by 90°, with the correlation shown in the following equation [21]:

$$I_L = \frac{V_L}{j\omega L} = \left(\frac{V_L}{\omega L}\right) e^{-j\pi/2} \tag{2.4}$$

Where I_L is the inductor current, V_L is the inductor voltage, L is the inductance, and $\omega = 2\pi f$ is the angular frequency. In an inductor

$$V_L(t) = -L\,\frac{di_L}{dt} \tag{2.5}$$

and therefore,

$$i_L(t) = i_L(t_1) + \frac{1}{L}\int_{t_1}^{t} v_L\, d\xi \qquad t > t_1 \tag{2.6}$$

Where $i_L(t_1)$ is the inductor current at time t_1 and ξ the variable of integration. Figure 2.4 shows an inductor with current $i_L(t_1)$ up to t_1, which changes at t_1 when a voltage of v_L is applied. Though the voltage changes instantaneously, the inductor current cannot change instantaneously.

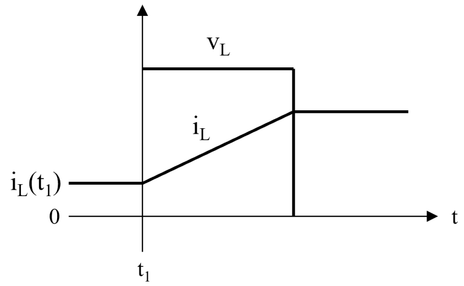

Figure 2.4: Relation between an induced voltage and the current in an inductor [21].

When considering a steady-state condition, the voltage waveform of the inductor repeats with a time period T, like $v(t+T) = v(t)$. When substituting $t = t_1 + T$ in Equation (2.6), and acknowledging that $i_L(t_1 + T) = i_L(T_1)$, the inductor operating under steady-state conditions results in

$$\frac{1}{T}\int_{t_1}^{t_1+T} v_L \, d\xi = 0 \tag{2.7}$$

Where ξ is again the variable of integration and v_L the inductor voltage. Equation (2.7) implies that in steady-state conditions, the average inductor voltage is equal to zero. This is illustrated in Figure 2.5, where area A equals area B. The integral of the inductor voltage is equal to the change in the inductor flux linkage, as is implied by Equation (2.7). It states that the net change of flux linkage over one time period is equal to zero, which is a necessary condition for a steady-state operation.

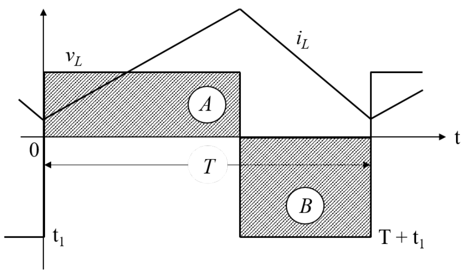

Figure 2.5: Inductor voltage and current response in steady-state conditions [21].

A way of measuring the performance of an inductor is with the quality factor, Q. The quality factor is defined as $Q = L\omega/R$, where L and R are the inductance and resistance, respectively, and $\omega = 2\pi f$, where f is the frequency, respectively. It is wanted to have a high quality factor since this would imply a low resistance in comparison to the inductance. As stated earlier, increasing the number of turns usually increases the inductance. The drawback of this approach however is that with an increasing number of turns, the series resistance of the conductor increases as well, since the conductor will both increase in length and, if the total area of the inductor stays the same, the conductor width will decrease. The inductance does add up when series-connected, meaning that multiple solar cells could be series connected to increase the inductance up to the desired value.

The equivalent circuit model of an integrated inductor is shown in Figure 2.6. The resistivity of the metal conductors is indicated with R_1, the coupling capacitances between the conductors and the substrate with C_{p1} and C_{p2}, and the resistances associated with the substrate and the metal conductors with R_{sub1} and R_{sub2}. With increasing frequency, the quality factor initially increases linearly, after which it drops at higher frequencies due to parasitic resistances and capacitances, and the skin and proximity effect [33].

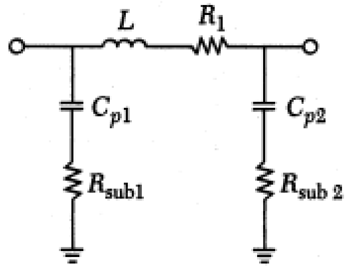

Figure 2.6: The equivalent circuit model for an integrated inductor [33].

In [12] several inductance values for different planar coil structures have been highlighted, like 3.13 μH for a 10 cm outer diameter inductor and 12.52 μH for a 13 cm outer diameter inductor.

2.5. DC-DC Boost converter

In DC-DC converters, the average output voltage can be controlled so that it equals the desired level. The input voltage and the output load may fluctuate. The boost converter, or step-up converter, is a power converter that increases the DC input voltage V_{in} to a higher output voltage V_{out}. The energy absorption and injection processes will make up a switching cycle, where the average output voltage is controlled by the switching on and off-time duration. Pulse-width modulation (PWM) is a method used to control the switching behavior, by chopping up the average power delivered by an electrical signal into discrete parts [38]. When the time integral of the voltage across the inductor (v_L) is zero, we are in a *steady-state operation*. The following *volt-second balance* is obtained [21]:

$$\int_0^{T_s} v_L\,dt = \int_0^{t_{on}} v_L\,dt + \int_{t_{on}}^{T_s} v_L\,dt = 0 \tag{2.8}$$

The following equation is obtained when applying Equation (2.8) to the boost converter,

$$V_{in}\,t_{on} + (V_{in} - V_{out})\,t_{off} = 0 \tag{2.9}$$

with the given that the switching duty cycle, D, is defined as

$$D := \frac{t_{on}}{T_s} \tag{2.10}$$

From the equations above the following definition is found

$$\frac{V_{out}}{V_{in}} = \frac{1}{1-D} \tag{2.11}$$

The boost converter will operate in two different modes, known as the continuous conduction mode (CCM) and the discontinuous conduction mode (DCM). The inductance is calculated to maintain the boost converter in a CCM, to maintain a stable output current. When the inductance is too small, the converter will operate in DCM, whereas if the inductance is too large, the converter becomes bulky and has a slow transient response. Since it is most of the time unwanted to operate a boost converter in DCM, due to high peak currents and RMS losses, this system is designed for CCM operation [39]. Such a CCM can be seen in Figure 2.7, where it is seen that the inductor current never reaches zero.

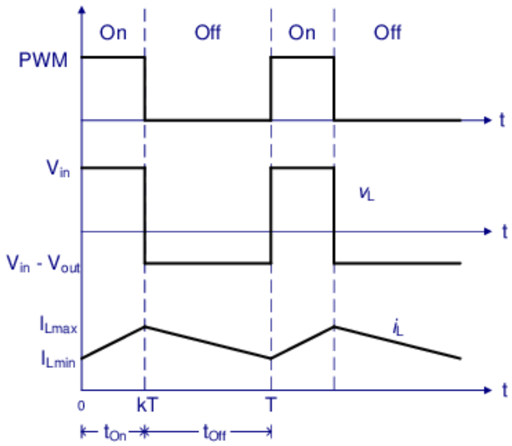

Figure 2.7: The PWM, the inductor voltage, and the inductor current from top to bottom [38].

For grid-connected PV systems, most of the time the boost converter is used for MPPT and connected to an inverter, which feeds into the low-voltage grid, where it is coupled to the medium-voltage grid using large 50 Hz transformers [40]. Fraunhofer has developed a high frequency (HF) SiC transistor power module with a switching frequency of 16 kHz, which can directly feed into the medium-voltage grid. They state that they can reach 10 times higher switching frequencies than other state-of-the-art silicon transistors [41]. By increasing the switching frequency of a power converter, the inductor can be decreased in size. The increase of frequency does however also increase the switching losses, thus reducing the converter efficiency [40]. In literature ([38, 39, 42]), a common switching frequency is found to be 20 kHz, though for this research higher frequencies are investigated. To find a matching inductance, the following equation is used [43]:

$$L = \frac{V_{in} D}{\Delta i_L f} \tag{2.12}$$

Where V_{in} is the input voltage of the boost converter, D the duty cycle calculated from Equation (2.11), Δi_L the current ripple, and f the switching frequency of the converter.

To acquire a minimum desired inductance value, the following two assumptions have been made; 1) the duty cycle is set to 0.5, and 2) the current ripple is 20% of the output current. The value for the duty cycle is chosen so that the output voltage of the DC-DC boost converter is twice the input voltage. The average range of the current ripple is between $10 - 30\%$, thus an average of 20% is chosen [43, 44]. Though these values are not ideal, this thesis investigates this specific case, after which in the future the assumptions can be altered.

The following data has been extracted from the datasheet of the *SunPower Gen 2 Cell - 160 mm*, which can be seen in Appendix A:

Table 2.1: Parameters *SunPower Gen 2 Cell - 160 mm*

Parameters	**Symbol**	**Value**
Open-circuit voltage	V_{oc}	0.677 V
Short-circuit current	I_{sc}	6.33 A
MPP voltage	V_{mpp}	0.575 V
MPP current	I_{mpp}	5.98 A

For this case, the input voltage and current of the DC-DC boost converter is set to the MPP voltage ($V_{mpp} = 0.575V$) and the MPP current ($I_{mpp} = 5.98A$), respectively. As stated above, the output voltage of the boost converter is twice the input voltage, thus resulting in an output voltage of $V_{out} = 1.15V$. A 20% input current ripple results in a value of $\Delta i_{PV} = 1.196A$.

When calculating the different inductance values needed for varying frequencies using Equation (2.12) and the data from the tables above, the following data is obtained:

Table 2.2: Inductance values for varying switching frequencies.

Frequency (kHz)	**Inductance** (μH)
10	24.04
20	12.02
100	2.40
200	1.20

2.6. Loss mechanisms

2.6.1. Resistive losses

When integrating planar inductors into c-Si cell designs, the conductor thickness has little influence on the value of the inductance, but it has a significant effect on the value of the series resistance of the coil[45]. Since the resistance through a conductor is inversely proportional to the cross-sectional area of the conductor, when decreasing the conductor thickness, the width needs to be increased to maintain the same resistance value. However, when decreasing the conductor thickness, with the increase in width, eddy currents can form and increase the winding losses at high frequencies [46]. These eddy currents occur because of the relative motion between the magnetic core of the inductor and the magnetic flux, as is presented in Figure 2.8 (a). Since air-core coils do not have a magnetic core, they are free of magnetic losses, like hysteresis. Hysteresis losses occur due to the reversal of the magnetic field and the retention property of the ferromagnetic core [47].

2.6.2. Skin effect

In the case of an increasing frequency in an AC system, due to the induced eddy currents, the current tends to become more distributed along the surface of the conductor. This means that the current density of a conductor in a high-frequency system is higher near the edge of the conductor and decreases exponentially with greater depths towards the center of the conductor. This phenomenon is called the *skin effect* since the current mainly flows on the 'skin' of the conductor. The phenomenon is shown in Figure 2.8 (a) and (b). The thickness of the layer on which the current flows is called the *skin depth*, δ, which is calculated with Equation (2.13).

$$\delta = \sqrt{\frac{2\rho}{\omega\mu}} \tag{2.13}$$

Where ρ is the resistivity of the conductor, ω is the angular frequency ($= 2\pi f$), and μ is the permeability of the conductor, which consists of the relative magnetic permeability of the conductor (μ_r) and the permeability of free space (μ_0).

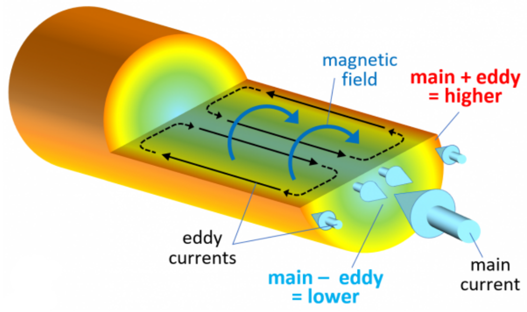

(a)

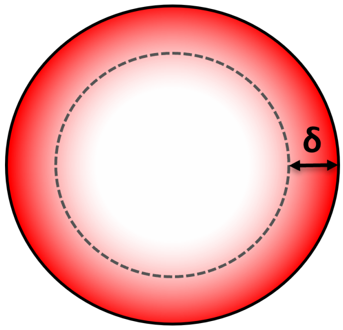

(b)

Figure 2.8: Illustration of the eddy currents induced in a conductor in (a) [48], and the cross-section of a conductor in (b), where δ indicates the skin depth.

A metal is a material that both has a non-zero conductivity, and has a relatively small skin depth. When examining the skin depth for copper at varying frequencies, where a maximum operating frequency of 200 kHz is taken from literature, the following depths are calculated [49].

Table 2.3: Skin depth at varying frequencies

Frequency (kHz)	**Skin depth** (μm)
10	650
20	460
100	206
200	145

Looking at Equation (2.13), when increasing the frequency of the system, the skin depth decreases, meaning that the same amount of current has to flow through a smaller cross-sectional area than at a lower frequency. This means that the resistance in the conductor also increases.

2.6.3. Proximity effect

Another loss mechanism in conductors is the *proximity effect*, which is an electromagnetic phenomenon that causes non-uniform current distribution in multi-turn windings or nearby conductors. It can lead to a significant increase in resistance, and thus power loss, like the skin effect. Due to the proximity effect, the currents that flow in the same direction seem to 'repel' each other (*direct proximity effect*), and the currents that flow in the opposite direction seem to 'attract' each other (*reverse proximity effect*). These two cases can be seen in Figure 2.9. Both the skin and proximity effect have a similar underlying cause, the induced eddy currents in the body of the current-carrying conductor, however, for the proximity effect these are induced because of the magnetic field from the nearby conductor penetrating the conductor perpendicular to the axis of the conductor. As can be seen from the top conductors in Figure 2.9, at the outer edges the direction of the eddy currents is the same as the main current, thus adding up to a higher local current density (indicated in reg). On the other edge, the direction of the eddy currents opposes the direction of the main current, therefore resulting in a lower local current density (indicated in green). Since the local power loss is proportional to the square of the local current density, even though the overall current density in the conductor stays the same, there will be an increase in power loss in the conductors experiencing the proximity effect [48].

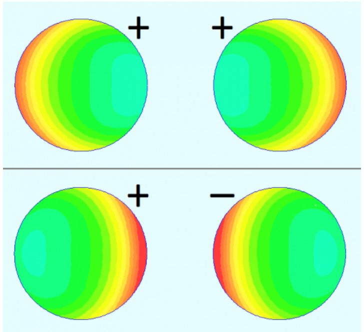

Figure 2.9: Proximity effect in two round wires, where the current in the top conductors flow in the same direction (equal phase), and the currents in the bottom conductors flow in the opposite direction (opposite phase).

3
Approach

In this chapter, the way that a planar inductor can be integrated into a c-Si solar cell is discussed. In Section 3.1 the so-called *coupled* approach method is explained, after which in Section 3.2 the *decoupled* approach is discussed.

3.1. Coupled approach

The integration of the planar coil onto the solar cell can be done in a couple of ways. Since the metal finger pattern on the front side of the FBC solar cell is carefully optimized for the shading and resistive losses, there is limited room for the integration of a planar inductor [13]. The backside of the FBC solar cell however has no shading losses (in case we are working with non-bifacial solar cells). In Figure 3.1 we can see two FBC cells, with the left image showing the backside of a normal n-type solar cell with a full metal back contact. The right image shows the so-called *coupled* approach, where the metal back contact is redesigned into a spiral-like pattern. By creating a back contact with a spiral-like shape, there is a possibility of increasing the self-inductance of the solar cell. This approach offers ease of integration, as there is a possibility that this can be done with little to no additional fabrication steps with respect to the standard production of c-Si cells. It should be noted that Equation (2.6) is not directly suitable for this solar integrated inductor, since the current through the metal conductor will increase towards the outer side of the coil, meaning a non-uniform current distribution across the inductor [12].

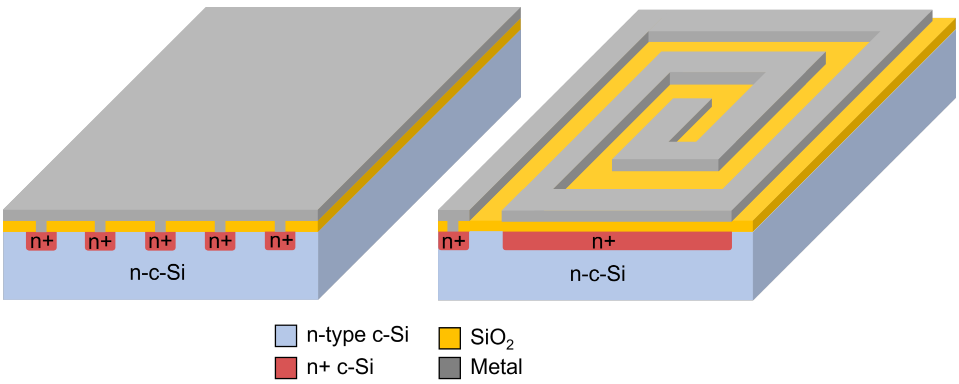

Figure 3.1: Sketch of a normal FBC cell on the left and an FBC with a possible re-designed back surface on the right.

3.2. Decoupled approach

The second method is the so-called *decoupled* approach, in which an insulator is placed between the charge carrier collection layer of the solar cell and the planar inductor. Depending on the type of converter that the inductor is applied in (buck, boost, or buck-boost), it will be either directly or indirectly connected to the solar cell. In case of a direct connection, as is the case in this thesis research, the insulator and the solar cell will have a direct point of contact through the hole in the insulating layer, as can be seen in Figure 3.2. This direct connection represents the series connection of the solar cell to the boost converter.

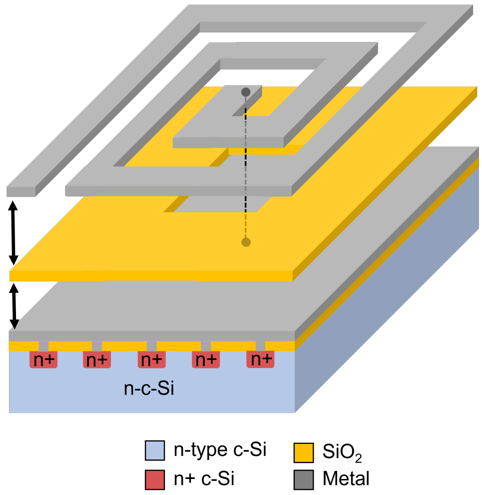

Figure 3.2: Sketch of an FBC cell with the decoupled approach.

The direct connected decoupled approach would still have the point contacts on the solar cell in order to reduce the defects of the metal-semiconductor interface [13]. This eliminates the property of the *coupled* approach in which the current is non-uniform and increases with each turn. It also allows both the charge carrier collection layer and the planar coil to be optimized separately, making it easier to increase the self-inductance of the cell. Since a planar inductor is added in series to the solar cell, the series resistance of the cell will increase, thus affecting the fill factor with respect to standard c-Si solar cells. Due to the insulating layer, the effect of the magnetic field on the solar cell is reduced in comparison to the previous method.

The decoupled approach will require extra fabrication steps in comparison to a regular solar cell, thus the cost-effectiveness will be affected. It is therefore desired to create a planar inductor that could be easily integrated into the production line of industrial c-Si solar cells.

By adding a magnetic material on one side of the planar coil, the inductance of the thin film inductor can increase by up to 200% [50]. This would mean that the air core inductor is made into a ferromagnetic core inductor, with the core on the outside of the inductor. This would most likely increase the manufacturing costs and the effects of the magnetic material on the solar cell are not yet clear and would have to be studied [12]. The insulator might even allow for a sandwich structure, where the inductor is encapsulated on both sides by a magnetic material [51]. Also for both approaches, the effect of parasitic resistances would need to be investigated, since parasitic resistances can lead to power dissipation resulting in possible temperature increases in the PV cell. This is however out of the scope of this research.

4
Models

This chapter explains the basics and in-depth computation behind the different models that have been created to simulate a planar inductor. The simulations were done in COMSOL Multiphysics®, which is a 3D simulation software used to create physics-based models and simulation applications. The software is based on the finite element method (FEM), which discretizes the partial differential equations (PDEs) into smaller, discrete parts.

For this research two different models have been created, a so-called *2D* and *3D model.* These two models have been used to compute two different approaches, which will be explained in Chapter 5 and Chapter 6. First, the parameters for both models are explained, after which their respective geometries and materials used are explained. Then the physics that form the backbone of the computation are discussed and lastly, the meshing applied to each model is explained. Since several parts of both the 2D and 3D models are the same, it is assumed that what is explained is applied to both models, unless explicitly stated otherwise.

4.1. Geometry

This section explains the model geometries, where first the coil geometry and later the air domain geometry are explained. For both the 2D and 3D models, the basic coil and air domain geometry are the same, thus will be explained once. However, the in-depth geometry is slightly different and will be explained individually.

4.1.1. Coil domain

In [45], different analytical expressions are compared to see which spiral geometry gives the highest inductance values. The geometries that are compared are square, circular, hexagonal, and octagonal. Of all the geometries, the square geometry gives the highest value of inductance. With the high inductance and the fact that the square coil is easy to model in COMSOL, this report only focuses on the production of a square planar inductor.

The parameters that influence the geometry are the number of turns (N), coil diameter (L), spacing (s), conductor thickness (t), and the conductor width (w), as can be seen in Figure 4.1.

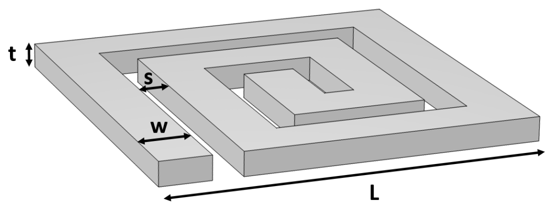

Figure 4.1: Example of a planar coil with the given coil diameter (L), spacing (s), conductor width (w), and conductor thickness (t).

For each number of turns, an Excel file is created which parametrizes the geometry of the coil, using just three parameters: L, s, and w. Both L and s are two parameters that can be set by the user, but w is dependent on both L and s as follows:

$$w = \frac{L - 2 \cdot N \cdot s}{2 \cdot N + 1}$$

Since the w is dependent on both the diameter of the coil and the spacing, the model always creates a coil that encloses the full given area for the given spacing and coil diameter. When comparing the inductance of such an inductor to one with the same area and turns but a larger spacing in the middle, the inductance of the latter is higher than the inductance of the former. However, one of the other objectives was to create a planar inductor that has a low enough resistance. For this reason, it is not only chosen to fully enclose the area of the cell but also the spacing is set at a constant value and as low as possible, increasing the conductor width and thus reducing the resistance. The chosen spacing value for both models was set at $s = 500\mu m$ since this is the lowest spacing value for which both models give a high enough minimum element quality. This assumption is confirmed when examining the quality factor of an arbitrarily chosen coil for a fixed frequency and thickness, but a varying spacing. The quality factor significantly reduces with increasing spacing, as can be seen in Table 4.1:

spacing (mm)	**quality factor**
0.1	4.4
0.5	2.6
0.9	0.6

Table 4.1: Quality factor as a result of varying spacing, for a coil of a fixed thickness ($10\mu m$) at 100 kHz.

The main reason for this decrease in quality factor with increasing spacing is that the resistance increases percentage-wise more than the inductance, thus decreasing the quality factor.

Table B.1 shows the first three turns of the file which was created for the parametrization of the coil geometry. Using an x- and y-coordinate, the coil is designed that with each increment, the data points go inward to the middle, after which they go out again to the outer point, creating a closed-loop coil. The starting height is indicated as $L/2 - N * w - N * s$. In the table, the yellow and orange parts indicate the added parts for each extra turn, where the base equation for each increment is the same, as can be seen in Table 4.2.

Table 4.2: Added data set for each turn increase, where N indicates the number of turns, w the width of the conductor and s the spacing between the turns.

xw	**yw**
-L/2+N*w+(N-1)*s	-L/2+(N-1)*w+(N-2)*s
-L/2+N*w+(N-1)*s	L/2-N*w-(N-1)*s
L/2-N*w-(N-1)*s	L/2-N*w-(N-1)*s
L/2-N*w-(N-1)*s	-L/2+N*w+(N-1)*s
L/2-N*w-N*s	-L/2+N*w+(N-1)*s
L/2-N*w-N*s	L/2-N*w-N*s
-L/2+N*w+N*s	L/2-N*w-N*s
-L/2+N*w+N*s	-L/2+(N-1)*w+(N-1)*s

Using these data sets for all the different turns, eight separate COMSOL files have been created ranging from one to eight turns. To create a coil geometry in COMSOL, a *Work Plane* was added to the *Geometry* node. A *Polygon* primitive was added to this *Work Plane*, and the data points from Table B.1 and **??** were implemented into this *Polygon* as coordinates, creating a 2D coil, as can be seen in Figure 4.2.

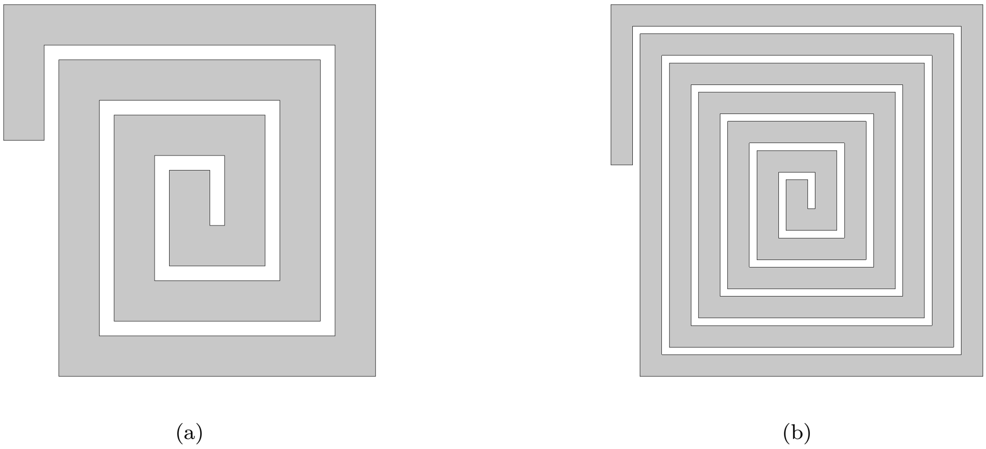

Figure 4.2: Top view of a 3-turn (a) and a 6-turn (b) coil.

Both models exist essentially out of 3 different layers: the *Upper layer*, the *Lower layer*, and the *Magnetic insulation layer*, of which the use of the latter will be further explained in Section 4.4. For the chosen physics interface in COMSOL, it is necessary to create a closed-looped system, as will be further explained in Section 4.4. To create a closed-loop system, the ends of the loop have to be connected. In the 2D model this is done by stacking the three different layers on top of each other in the *Materials* branch (Section 4.3), thus creating a virtual 3D model, as can be seen in Figure 4.3.

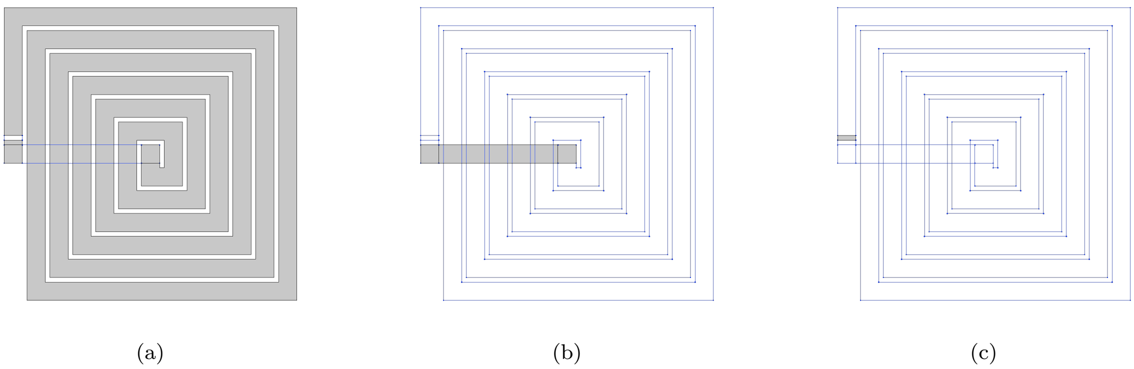

Figure 4.3: Top view of a 6-turn coil, where (a) shows the *Upper layer*, (b) the *Lower layer*, and (c) the *Magnetic insulation layer* for the 2D model.

For the 3D model a full 3D coil has to be modeled, with not just the Upper, Lower, and Magnetic insulation layers, but also the vertical conductors to connect the different layers, as can be seen in Figure 4.4.

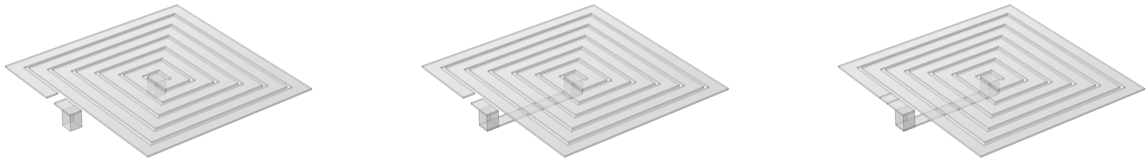

(a) (b) (c)

Figure 4.4: Top view of a 6-turn coil, where (a) shows the *Upper layer* with the vertical conductors, (b) with the added *Lower layer*, and (c) with the added *Magnetic insulation layer* for the 3D model.

4.1.2. Air domain

To compute the magnetic field lines, an air domain has to be modeled around the coil. This air domain is equal for both models. For the models, a spherical air domain shape was chosen, since this most closely resembles the shape of the magnetic field lines, as can be seen in Figure 4.5 (a). A sphere domain with given radius can be seen in Figure 4.5 (a).

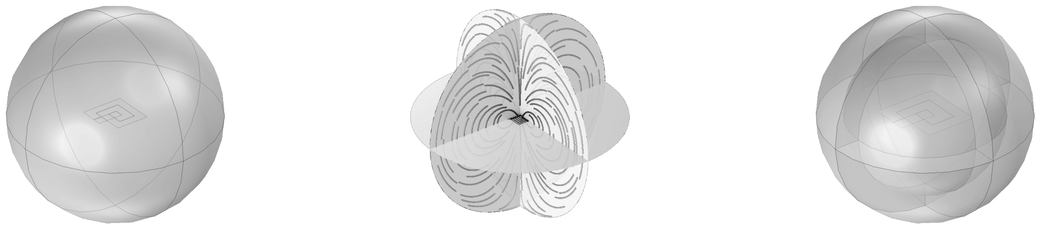

(a) (b) (c)

Figure 4.5: Spherical air domain with no added layer (a), the magnetic field lines of a planar inductor in a spherical air domain (b), and a spherical air domain with an added layer (c).

With increasing sphere size, the solution time will increase too. A too small sphere radius and the solution will be inaccurate. For this reason, a parametric sweep has been applied over the radius of the sphere, which can be seen in Table 4.4.

Table 4.3: Inductance and resistance values for varying sphere radii.

Radius (cm)	**L** (μH)	**R** (mΩ)
15	1.1418	1.9027
30	1.1780	1.9027
45	1.1816	1.9027
65	1.1826	1.9027
100	1.1829	1.9027

It can be seen in Table 4.4 that the biggest sphere gives the highest inductance. The resistance is the same everywhere since this is only measured in the coil, which does not change. The inductance L

in COMSOL is defined by the current flowing through the system (I) and the magnetic energy density (W_m), of which the latter is proportional to the magnetic field square (B^2) [52]. The inductance can be measured by integrating the magnetic energy density over the entire geometry and dividing this by the current squared, as follows [53]:

$$L = \frac{2}{I^2} \int_{\Omega} W_m \, d\Omega \tag{4.1}$$

Where L is the inductance, I is the current in the coil, and W_m is the magnetic energy density. It is expected that with increasing air domain, the inductance will increase. To create a model which closely represents real life, it is important to be able to model all the physics. If we were to create a model that has a domain that would contain all the magnetic field lines, the model would become too big, significantly increasing the solution time. According to the Biot-Savart law, the magnetic field is inversely proportional to the distance, thus decreasing with increasing distance from the coil. Since these magnetic field lines at very long distances are very small, they have a limited impact on the outcome values of the model. For this reason, an *Infinite Element Domain* (IED) is introduced. The IED is a property in COMSOL which is applied to the outer edges of the air domain, as can be seen in Figure 4.5 (c).

The IED is applied in an outward radial direction from the edges of the air domain and resembles an infinite domain. It does so by stretching the finite elements on the edge of the physical domain in the radial direction to a very large distance from any region of interest. The default physical width of the stretching is $1e3 * dGeomChar$ meter, where $dGeomChar$ is the pole distance chosen by COMSOL. This leads to an infinite element domain that is very large compared to the geometry dimensions with nearly a $1/r$ stretching [54].

Table 4.4: Inductance and resistance values for varying sphere radii. The sphere without an IED is compared to a sphere with an IED.

Radius [cm]	Remark	L [μH]	R [mΩ]
15	no IED	1.1418	1.9027
15	IED, 5cm layer	1.1829	1.9027
30	no IED	1.1780	1.9027
30	IED, 5cm layer	1.1832	1.9027
45	no IED	1.1816	1.9027
45	IED, 5cm layer	1.1831	1.9027
100	no IED	1.1829	1.9027

The table shows that the IED has a significant effect on the inductance. For both the 2D and 3D model, a sphere with a radius of 15 cm and a 5 cm IED layer is chosen, since it has an equal value as a sphere radius of 100 cm, a very small difference ($< 0.03\%$) from larger sphere radii with IED, and the smallest solution time.

4.2. Parameters

Using parameters to create and control a model in COMSOL, is one of the ”most powerful and easy-to-use feature of the COMSOL Multiphysics® software”. With increasing model complexity, it is common that there is an increase in parameters, giving the user more overview of their model. It also allows for *parametric sweeps*, which is a feature in COMSOL that allows solving several variations of the model without changing the variations manually [55]. Since this model also has a high complexity and a need for parametric sweeps, the following set of parameters was introduced to both models, of which several are already mentioned in Section 4.1.

- Number of turns (N): the total number of turns that the coil has.

- Coil diameter (L): the total diameter of the coil, taken at its smallest point.
- Spacing (s): the space between two consecutive turns of the coil, where the spacing cannot be greater than $\frac{L}{2 \cdot N}$, for else the inductor, will not fit on the given area.
- Conductor thickness (t): the thickness of the conductor.
- Conductor width (w): the width of the conductor.
- Input current (I): the excitation current of the coil.
- Sphere radius (R_sp): the radius of the sphere of the surrounding domain.
- Thickness radius sphere (t_sp): the thickness of the layer of the sphere.

4.3. Materials

The *Materials* branch allows the user to define different materials for different sections of the model. In this case, the model exists out of three different materials: a metallic material for the conductor, an insulator for between the different layers of the conductor, and air for the surrounding domain. When the model is extended with for instance a metallic plate for increasing the inductance, a material has to be appointed to this domain as well. A large number of preset materials are available in COMSOL with their respective properties. With the *Material Library* spanning a wide range of materials, like Elements, Alloys, Semiconductors and Optic Materials, and many more, a total of 10,328 preset materials can be chosen in COMSOL [56].

There are two different *Materials* branches in the COMSOL software, one under the *Global Definitions* branch and the other under the *Component* branch. For the 2D model, a set of materials (copper, FR4 (Circuit Board), and air in this case) were chosen in the *Global Definitions* branch. In the same branch, a set of *Layered Materials* is created, named *Upper metallization*, *Lower metallization*, and *Vias metallization*. Each layer is given the material property of copper in this case, with a certain thickness *t_cond*.

In the *Materials* branch in the *Component* branch, the following four different 2D layered material stacks are created: *Upper metallization*, *Lower metallization*, *Intersections*, and *Vias*.

The *Upper metallization* stack is made up of the *Upper metallization* layer with an insulator underneath it. The *Lower metallization* stack is just the *Lower metallization* layer. The *Intersections* stack consists of the *Upper metallization* layer under which an insulator for the intersections is placed which is on top of the *Lower metallization* layer. The *Vias* stack is also made out of three materials from the *Global Definitions* branch, namely the *Upper metallization* layer, the *Vias metallization* layer, and the *Lower metallization*. The four different stacks can be seen in Figure 4.6.

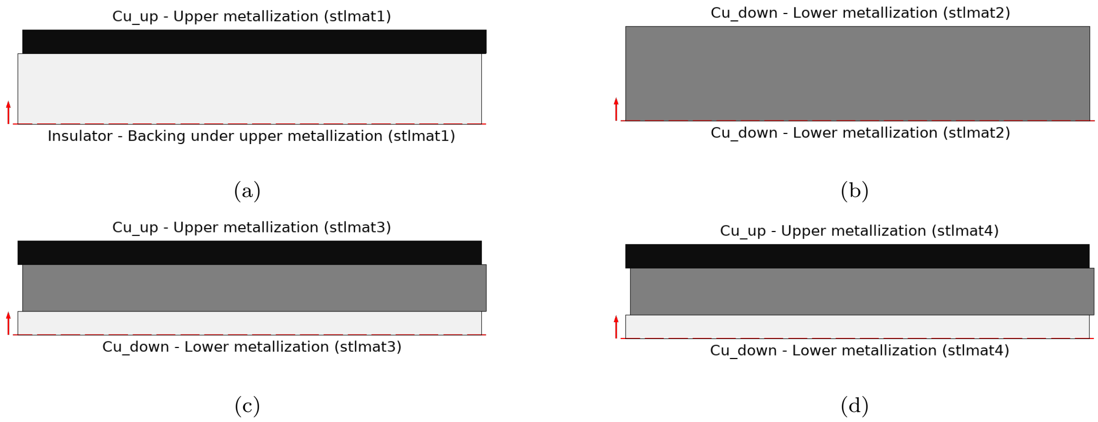

Figure 4.6: Side view of the four different stacks for the 2D model, where (a) shows the *Upper metallization* stack, (b) the *Lower metallization* stack, (c) the *Intersections* stack, and (d) the *Vias* stack.

For the 3D model, only the *Materials* branch in the *Component* branch is used, where the different materials are manually assigned to the geometry of the coil. In this case, the coil was assigned the material copper, the insulator FR4 (Circuit Board), and the air domain the material air.

4.4. Physics

This section sheds some light on the physics that have been used for the models. First, the *Magnetic Fields* interface is discussed, which has been used for both models. Afterward, the *Electric Currents in Shells* interface is discussed, which is only applied to the 2D model.

4.4.1. Magnetic Fields

For both models, the same generic physics interface was used. This physics interface is the *Magnetic Fields* (*mf*) interface in COMSOL and "it is used to compute magnetic fields and induced current distributions in and around coils, conductors, and magnets" [57]. The governing equations are the Maxwell equations. These equations are formulated using the magnetic vector potential in the air domain, and the magnetic vector potential and scalar electric potential in the coil domain.

The first node of the *mf* interface is the *Ampère's Law* node. The magnetic vector potential is added to the air domain using this node, which is applied to the entire surrounding air domain. The second node, the *Magnetic Insulation* node, is then applied to the outer domain (including the IED domain), which is the default boundary condition for the *mf* interface. It sets the tangential component of the magnetic potential at the boundary to zero.

The 2D model then has two nodes applied that are not present in the 3D model. These are the *Surface Current Density*, which is a boundary condition applied on the coil which specifies a surface current density. This surface current density is obtained from the other interface (*Electric Currents in Shells* interface) applied to the 2D model to connect both physics interfaces. The other node is the second *Magnetic Insulation* node, which is now applied to the *Magnetic insulation layer* from Figure 4.3 (c). In this case, it specifies that at the edges of the chosen part of the coil, the magnetic potential is zero, thus creating an insulator between the beginning and the end of the coil. The excitation of the 2D coil will be discussed in Section 4.4.2.

For the 3D model, the *Coil* node is applied to the coil domain, giving COMSOL the notice that the shape created in the *Geometry* node is a coil. All the options in COMSOL, like the material property relationships (permeability, permittivity, conductivity, ...), are from the *Materials* branch. The preset excitation value is a 1 Ampere current excitation, though this can be easily adjusted into a different value or type of excitation. For the 3D model, the excitation was *1 Ampere*, which was assigned to the *I_1* parameter. The *Coil* node has a drop-down sub-feature called *Geometry Analysis*, with additional sub-features to it. One of those sub-features is the *Input* feature, which specifies where we want the current to flow into the coil. Figure 4.7 shows the point of excitation of the coil for the 3D model.

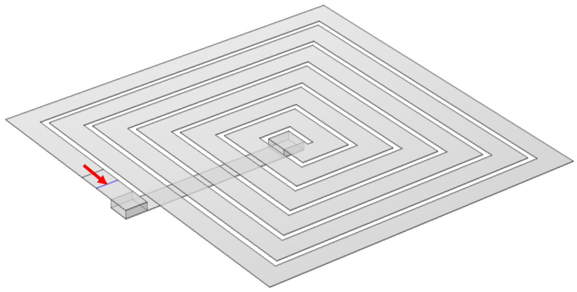

Figure 4.7: Coil geometry where the red arrow indicates the starting point of the current excitation.

4.4.2. Electric Currents in Shells

The *Electric Currents in Shells* (*ecis*) physics interface is only applied for the 2D and is used to compute electric fields, currents, and potential distributions in thin layered materials, where the inductive effects are negligible. This indicates that this interface is only applicable when the skin depth is larger than the coil thickness [58]. For that reason, the skin effect is not taken into account for the 2D model. For increasing frequencies, the skin depth decreases, thus limiting the range of this model, which will be further explained in Section 4.8.

4.5. Mesh

As explained in the chapter introduction, COMSOL can be described by partial differential equations (PDEs) and the solution to the mathematical model is approximated through the finite element method (FEM), on which the COMSOL software is based on. The FEM is used to discretize the problem, thus divide and conquer the model. Discretizing the problem means breaking it down into smaller, discrete parts. These parts are called elements and the solution is obtained by stitching together lower-order polynomials over each element to form a piece-wise global function. The quality of the mesh is expressed in a value between 0 and 1, where 1 indicates the highest mesh quality and 0 the lowest. Though the COMSOL meshing algorithm tries to avoid elements with low quality, it is not always possible to do so. A rule of thumb, and also applied in this research, is to keep the minimum element quality higher or around 0.1 [59].

There are two different meshing types available in COMSOL; *Physics-controlled* and *User-controlled* mesh. The *Physics-controlled* mesh is the default meshing sequence in COMSOL and lets the software determine the meshing sequence according to the physics. This means that with changing physics, there will be a change in meshing too. The mesh element size can be globally adjusted using the *Element size* drop-down menu from the *Mesh* node, giving a range of nine predefined sizes from Extremely coarse up to Extremely fine. Finer mesh size elements will give a more accurate result, but will make the problem more computationally expensive and will increase the solution time.

The *User-controlled* mesh sequence allows the control of the mesh using mesh nodes. This can be done by changing the meshing sequences, like size and distribution, and the mesh elements. In 2D models, the mesh elements can be divided into triangles or quadrilaterals, where the first is the default element used. In 3D models, the mesh elements can be divided into tetrahedrons, hexahedrons, pyramids, and prisms, where the default are the tetrahedral elements.

For the 2D model, a *Physics-controlled* mesh is chosen since this gave a high enough mesh quality without creating a too computationally expensive model. For the 3D model, a *User-controlled* mesh sequence was created, since the *Physics-controlled* mesh failed to create a mesh fine enough to model the skin effect and stay computationally light. The 3D meshing was divided into three parts: the coil, the air domain, and the IED, as can be seen in Figure 4.8.

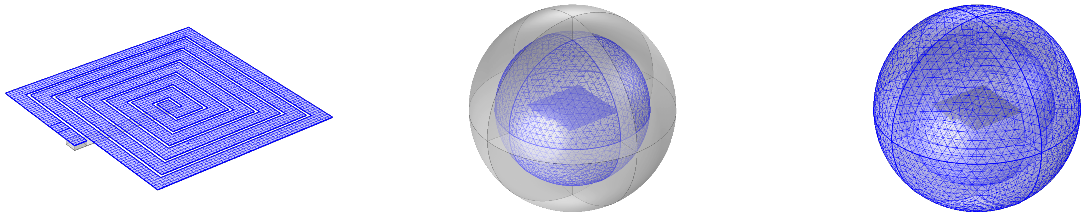

(a) (b) (c)

Figure 4.8: The meshing of (a) the coil, (b) the air domain, and (c) the IED.

For the 3D model COMSOL not just has to mesh the upper 2D plane, but also the spacing between the conductor and the conductor below the coil. Since the spacing is very small, the meshing algorithm has difficulty meshing these areas. To keep a minimum element quality of around or greater than 0.1, two extra planes are added in the *Geometry* branch, fully enclosing the coil. These planes are then extruded to the same width of the coil, initially creating one large square plane. In the *Materials* branch, the two added planes are however given the material property of air, virtually creating the spacing between the conductors. The meshing can be seen Figure 4.9.

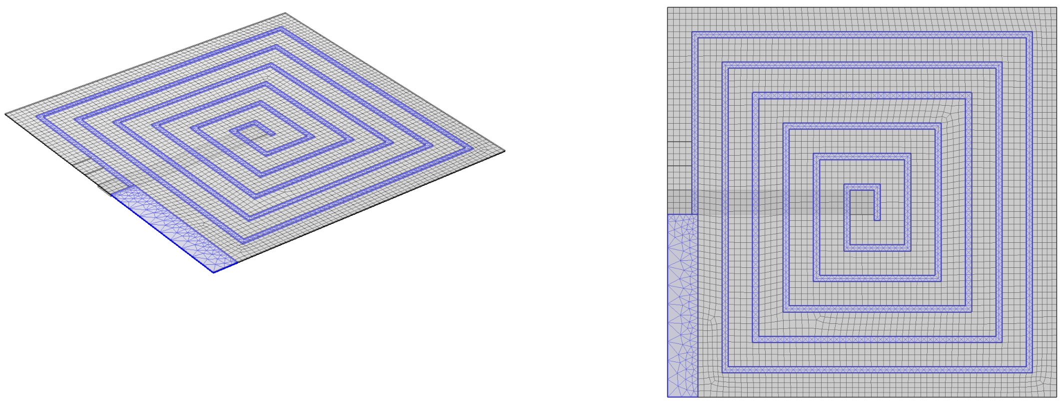

(a) (b)

Figure 4.9: The meshing of the 3D coil from (a) the side, and (b) the top, with the extra planes indicated in blue.

4.6. Study

For this research, two different studies have been conducted: the *Stationary* study and the *Frequency Domain* study, where the first represents a steady-state DC system and the latter a steady-state AC system. Both studies will be further explained in the following subsections.

4.6.1. Stationary

The *Stationary* study represents a steady-state DC condition of the system, where field variables do not change over time. With the *Stationary Solver* node, the solution to linear and non-linear stationary problems is found. It is also used for optimization problems that are constrained by a stationary PDE [60].

4.6.2. Frequency Domain

The *Frequency Domain* study is used to create a model which is subjected to an excitation of a certain set frequency. For the Frequency Domain study, the current consists of a conduction current and a displacement current. The former scales with the conductivity and the latter scales with the frequency. For low frequencies, as is the case in this research, the conduction will be dominant. As such, if the conductivities in various domains differ by too many orders of magnitude, the linear problem becomes numerically unstable. For that reason, for the Frequency Domain study, the conductivity of the surrounding air domain is assigned an arbitrarily non-zero value of 1000 S/m, which is still far lower than the conductivity of the copper coil [61].

4.7. Series resistance

Since we are connecting the planar inductor in series to the solar cell, we want to keep the added series resistance (R_s) to a minimum while still adding a high enough inductance to the cell. To set boundaries for the added series resistance, this research focuses on a specific solar cell. This solar cell is the *SunPower Gen 2 Cell - 160 mm* for which the IV and PV curves have been plotted in a SPICE-based analog electronic circuit simulator called LTSpice [62]. The parameters that were not on the datasheet of the solar cell have been obtained using the estimation methods proposed [63], such as the series resistance (4.3 $m\Omega$) and shunt resistance (132.27 Ω) of the solar cell.

By plotting multiple PV curves for increasing series resistances with increments of 0.1 $m\Omega$ from the original series resistance up to 10 $m\Omega$, the following PV plot can be seen:

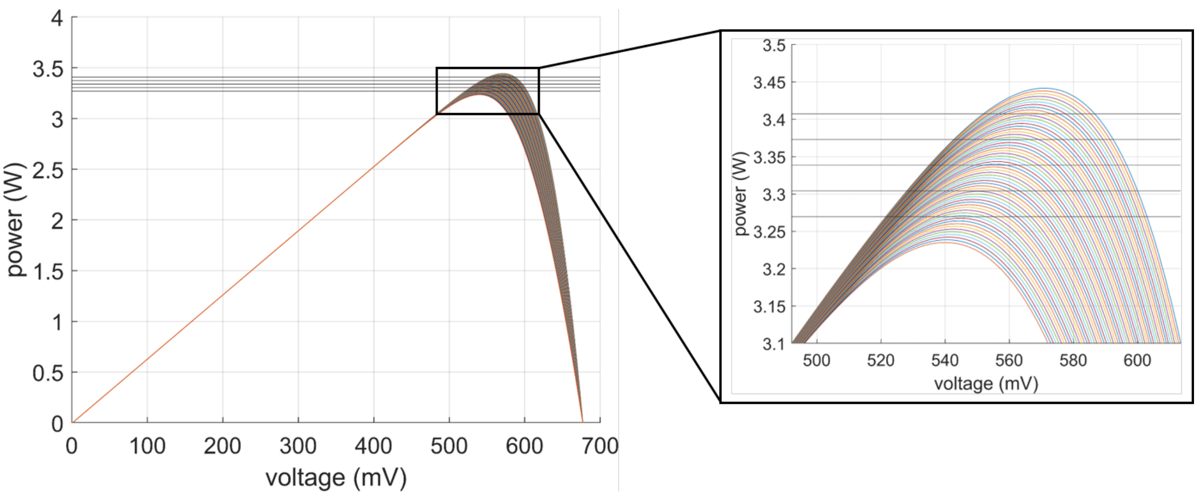

Figure 4.10: PV curve of a solar cell, with the horizontal lines indicating the five different maximum power loss values.

The graph above shows the multiple PV curves for increasing series resistances indicated by the colored lines. Going down each curve from above indicates an added series resistance of 0.1 $m\Omega$ to the original series resistance of the solar cell. The horizontal lines indicate the maximum power values for varying percentage losses. Thus, the top horizontal line indicates a 1% power loss from the original P_{mpp}, the second a 2% power loss, and so on.

In the following table, the set of five different power losses is proposed and their respective allowable added series resistance. The tolerance (Δ) shows the absolute difference between the maximum power for the given percentage and the maximum power from the PV curve. The maximum power for the given percentage is obtained by $P_{max} \cdot (1 - \%)$, where $P_{max} = 3.442$ W [62].

Table 4.5: Added series resistance (R_{as}) for varying power loss percentages with a 100% power of 3.442 W

P_{loss} (%)	$P_{max,new}$ (W)	Δ	R_{as} (mΩ)
1	3.4072	0.0016	1.0
2	3.3728	0.0003	2.0
3	3.3384	0.0014	2.9
4	3.3040	0.0004	3.9
5	3.2695	0.0015	4.8

Depending on the allowed power loss, the added series resistance can be in the range of 1.0 to 4.8 $m\Omega$. When series connecting multiple cells, a higher added series resistance is allowed. For instance, if we would series connect 16 cells with a maximum power loss of 5%, we can have an added series resistance of 16 times 4.8 $m\Omega$ which would be 76.8 $m\Omega$.

When examining the current density inside the square planar coil for a Stationary study, as can be seen in Figure 4.11, a uniform current density is seen at the straight parts of the coil. However, the corners, and especially the most inner, first 90° corner, show a less uniform current density. This increases the resistance of the coil, so to reduce the resistance of the coil, a different shape, like hexagonal or circular, coil should be used. However, this is out of the scope of this thesis.

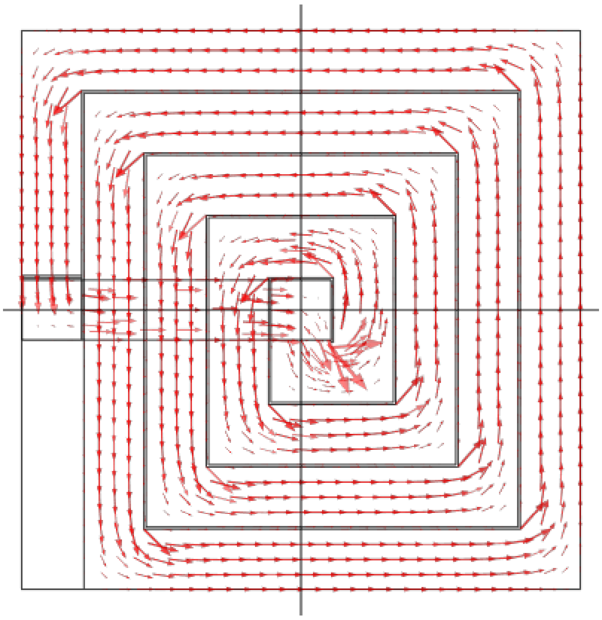

Figure 4.11: Top view of the current density of a 4-turn square planar coil during a Stationary study.

4.8. 2D versus 3D model

Since the 2D model is only applicable when the inductive effects are negligible, thus for thicknesses smaller than the skin depth, it is expected that with increasing frequency and coil thickness, the 2D model starts to show deviating results from what is expected, whereas the 3D model will show the expected results. The advantage of the 2D model, however, is that the model allows for smaller thicknesses and a lower solution time. Due to the explained meshing in Section 4.5, the minimum conductor thickness for the 3D model is 400 μm, since this is a thickness where there is still a mesh with a high enough quality. Therefore, the 2D model is used up to a thickness of 300 μ and the 3D model from 400 μm and up. The inductance and resistance values for a range of thicknesses and frequencies can be seen in Appendix C.

4.9. Magnetic material

The decoupled approach allows for the addition of a magnetic material, where it is known that with the addition of a magnetic material, the inductance will increase [64]. The addition of a magnetic material can be done in a single or sandwich structure, see Figure 4.12, where the single structure implies adding a magnetic material to one side of the coil, and the sandwich structure to both sides of the coil. To validate the assumption of a 200% increase in inductance, a 3-turn coil with a gap of 0.5 cm between a *Soft Iron (Without Losses)* magnetic material is simulated.

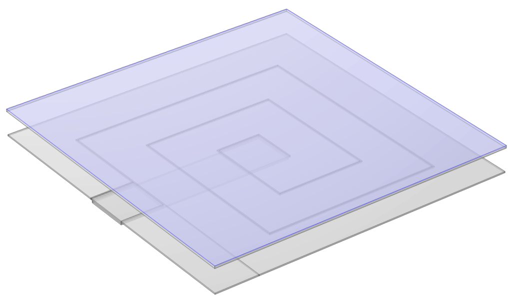

(a)

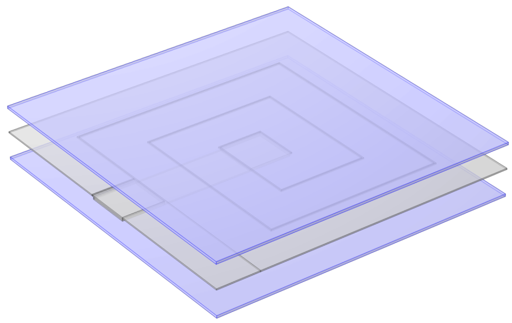

(b)

Figure 4.12: Planar coil with (a) a single magnetic material, and (b) a sandwich of a magnetic material.

The inductance and resistance values for a 3D model with 3 turns and a thickness of 500μm are 0.524μH and 1.411$m\Omega$, respectively. When comparing this to the inductance value when adding a magnetic material, there is an inductance increase of 47% for the single structure and even a 203% increase for the sandwich structure in a Stationary study. When only examining the sandwich structure for the Frequency Domain study, the inductance has a percentage increase ranging from 203% for a 1 Hz frequency up to a 12% increase for the 100 kHz frequency. This shows that even though the percentage increase decreases with increasing frequency, there is still a lot to gain from adding a magnetic material and shows a promising direction for further research. The results show that the 200% inductance increase is valid, and will therefore be used in this research too, though further research into the effects on the solar cell and the actual achievable inductance increase is needed.

5
Screen Printed Coil(s)

This chapter will investigate the feasibility of implementing a planar inductor into the fabrication process of a c-Si cell using a screen printing method. After a set of assumptions that gave the research some boundaries, the results are shown for a single coil application, and afterwards for multiple coils per cell.

5.1. Assumptions

5.1.1. Production process of a c-Si cell

When comparing traditional coil-forming methods to screen-printed coils, the latter enables rapid fabrication of lighter, durable, and flexible coils [65]. The decoupled approach, where the coil is separated from the cell, requires additional processing steps compared to the regular fabrication processes of PV cells. As such, it is most likely not cost-effective to implement planar coils on too many cells in the module. A cost-benefit analysis would shed more light on this, but this is out of the scope of this research. However, for the coupled approach, the planar inductor is directly integrated into the c-Si solar cell and could be integrated into the fabrication process of the cells. The current distribution in the coupled approach coil is non-uniform, possibly increasing the difficulty of the simulation, though this is out of the scope of this research. However, it would be an advantage if we can still make use of the tools that are common in solar cell production lines, thus the achievability of the screen-printed coils is investigated.

As stated, for this method the production of the special cells (*PV cells with integrated planar coil*) is integrated into the fabrication process of normal PV cells using the screen printing method. This will limit the maximum thickness of the coil. In literature, several thicknesses are found, in the range of 5 to 9 μm for single and 35 to 225 μm for multiple screen printed layers [66–70]. For this approach, a minimum thickness of 10 μm and a maximum thickness of 200 μm is used.

The added series resistance depends on the desired power loss percentage, but as shown in Table 4.5 ranges between 1.0 $m\Omega$ for a 1% power loss and 4.8 $m\Omega$ for a 5% power loss.

5.1.2. Only 2D model

As stated in Section 4.8, the 2D model is used for thicknesses lower than 300 μm. Therefore, this approach will solely be examined using the 2D model, with a thickness ranging from 10 to 200 μm. At the maximum frequency of 200 kHz, the skin depth is 145 μm, which would imply that the thickness of the conductor is still smaller than twice the skin depth, and thus the skin effect would not play a role. To check whether the assumption is correct, a 3D model of a straight wire in an air domain is created, where the current density distribution and resistance are obtained for varying thicknesses and frequencies, with a fixed width of 4 cm, which is the maximum width for all the number of turns. A straight wire is used, and not a single circular planar coil for instance, since this will discard the proximity effect of any nearby wire (or the same wire on 'the opposite side').

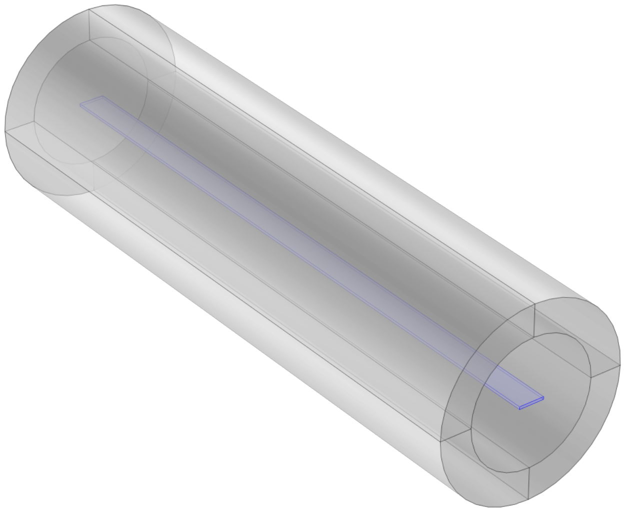

Figure 5.1: View of the 3D model of the straight conductor indicated in blue ($t = 200\mu m$, $s = 500\mu m$, and $w = 4cm$) in an air domain with an IED.

In a DC system, it is expected that with an increase from 200 μm to 1000 μm, the resistance will increase five times, since the resistance scales linearly with the thickness. When inspecting Table 5.1, it can be seen that this is indeed the case for the DC system, but that with increasing thickness the difference between the 200 μm and 1000 μm resistance decreases significantly, indicating a higher increase in resistance for the 1000 μm conductor than for the 200 μm conductor. The different frequency phases can also be seen in Appendix D. From the data in Table 5.1 and Appendix D, it is visible that the first assumption that no skin effect would take place at low thicknesses is incorrect. The table shows a slight increase in resistance for lower frequencies (up to 10 kHz) and even a 68% increase of resistance for a frequency of 200 kHz. The figures in Appendix D show an increase of current density towards the outer edges of the conductor and a decrease in the center, indicating that the skin effect does take place at lower frequencies.

Table 5.1: Resistance values for the 3D straight wire model for the Frequency Domain study for a thickness of 200 and 1000 μm. Δ indicates the difference between $R_{200\mu m}$ and $R_{1000\mu m}$.

f (kHz)	$\mathbf{R}_{200\mu m}$ $(m\Omega)$	$\mathbf{R}_{1000\mu m}$ $(m\Omega)$	Δ
DC	104.75	20.951	5.00
1	104.84	21.323	4.92
10	110.97	29.048	3.82
100	153.95	71.978	2.14
200	176.17	102.51	1.72

In the 2D model, the skin effect is however not taken into account by the COMSOL software due to the *ecis* physics interface. Despite the deviating results from reality, the *screen printed* approach is still examined using the 2D model to see if the screen printing method would be feasible in the best-case scenario. If that is not the case, then it will not be feasible in a real-life situation either.

5.2. Results

The resistance and inductance values for the varying conductor thicknesses are shown in the following tables.

Table 5.2: Resistance values for the 2D model during Stationary study. The thickness ranges from 10 to 200 μm, for all number of turns with a spacing of 500μm on a 12.5 cm cell.

t (μm)	N	R ($m\Omega$)	N	R ($m\Omega$)	N	R ($m\Omega$)	N	R ($m\Omega$)	N	R ($m\Omega$)	N	R ($m\Omega$)	N	R ($m\Omega$)	N	R ($m\Omega$)
10	1	7.06	2	31.23	3	68.86	4	120.17	5	185.63	6	265.02	7	358.59	8	466.51
20	1	3.53	2	15.61	3	34.43	4	60.14	5	92.81	6	132.51	7	179.3	8	233.26
30	1	2.36	2	10.41	3	22.96	4	40.10	5	61.88	6	88.34	7	119.54	8	155.51
40	1	1.77	2	7.81	3	17.22	4	30.07	5	46.41	6	66.26	7	89.65	8	116.63
50	1	1.14	2	6.25	3	13.77	4	24.06	5	37.13	6	53.01	7	71.72	8	93.31
100	1	0.71	2	3.12	3	6.89	4	12.03	5	18.57	6	26.51	7	35.87	8	46.66
200	1	0.35	2	1.56	3	3.45	4	6.02	5	9.29	6	13.26	7	17.94	8	23.33

Table 5.3: Inductance values for the 2D model during Stationary study. The thickness ranges from 10 to 300 μm, for all number of turns with a spacing of 500μm on a 12.5 cm cell.

t (μm)	N	L (μH)	N	L (μH)	N	L (μH)	N	L (μH)	N	L (μH)	N	L (μH)	N	L (μH)	N	L (μH)
10	1	0.056	2	0.236	3	0.523	4	0.916	5	1.414	6	2.017	7	2.725	8	3.537
20	1	0.056	2	0.236	3	0.523	4	0.916	5	1.414	6	2.017	7	2.725	8	3.537
30	1	0.056	2	0.236	3	0.523	4	0.916	5	1.414	6	2.017	7	2.725	8	3.537
40	1	0.056	2	0.236	3	0.523	4	0.916	5	1.414	6	2.017	7	2.725	8	3.537
50	1	0.056	2	0.236	3	0.523	4	0.916	5	1.414	6	2.017	7	2.725	8	3.537
100	1	0.056	2	0.236	3	0.523	4	0.916	5	1.414	6	2.017	7	2.725	8	3.537
200	1	0.057	2	0.236	3	0.523	4	0.916	5	1.415	6	2.017	7	2.725	8	3.537

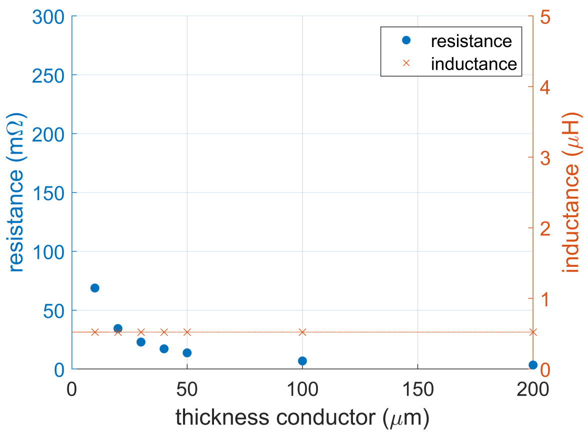

(a) 3 turn

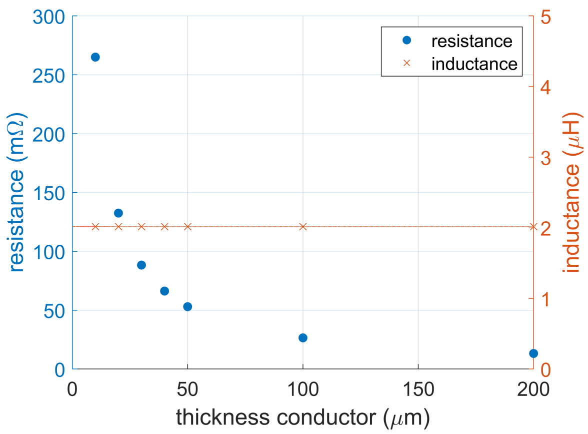

(b) 6 turn

Figure 5.2: Both the resistance and inductance values were plotted against the conductor thickness for (a) 3 turns and (b) 6 turns. The dashed line shows the constant values of the inductance.

When investigating the results from Figure 5.2, a constant inductance, but a decreasing resistance is seen per increasing conductor thickness for both turns. This is also the case for all the other turn values, as can be seen in Table 5.3 and Table 5.2. For that reason, it is desired to choose the largest thickness for the integration of a planar inductor onto a c-Si cell, which is 200 μm. The following plots show the inductance and resistance values for different turns with a fixed conductor thickness of 200μm.

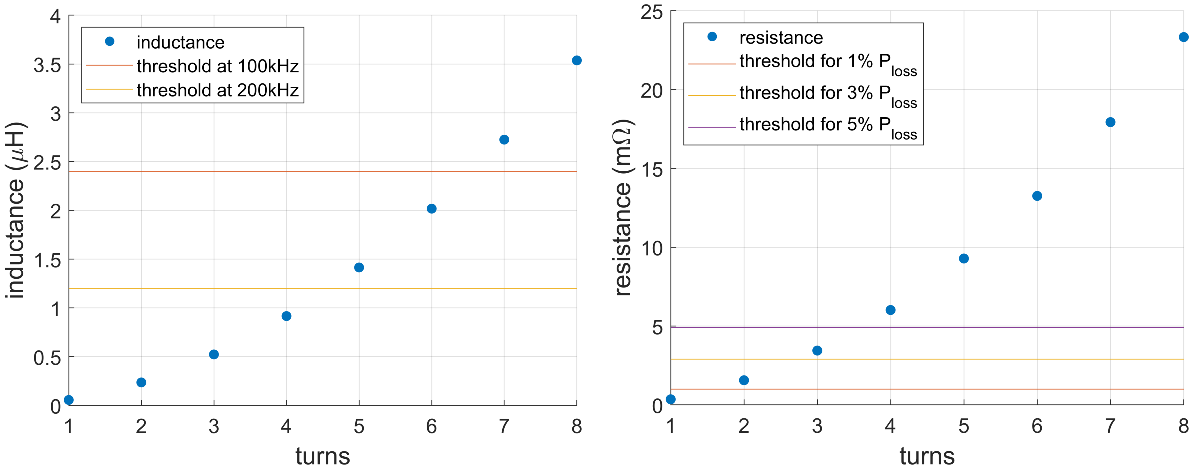

(a) (b)

Figure 5.3: Plots of the inductance (a) and resistance (b) for varying turns with a fixed thickness of 200 μm. Plot (a) shows the coil inductance and the threshold values for 100 kHz and 200 kHz. Plot (b) shows the coil resistance and the maximum allowed added series resistance for varying power loss percentages.

Examining Figure 5.3 (a), it can be seen that for an operating frequency of 100 kHz, the needed inductance for the system is too high for all but the 7 and 8-turn coils. When increasing the frequency to 200 kHz, this increases up to four inductors, showing that for this frequency a coil of 5 turns could still be used. When comparing the inductance analysis to the maximum allowed resistance values shown in Figure 5.3 (b), the 5-turn coil resistance value does not fall below the threshold value for the 5% power loss. These two plots show that a single coil does not create a high enough inductance or a low enough resistance for c-Si solar cell integration for a 5% power loss and a thickness up to 200 μm. There is the possibility of adding a magnetic material, which can boost the inductance by 200% [50]. If the inductance of all the coils are boosted, coils above the 3-turn for a 100 kHz and all coils above the 2-turn for a 200 kHz frequency will exceed the inductance threshold of 2.40 μH and 1.20 μH, respectively. When comparing this to the resistance values, only the 3-turn coil for a 200 kHz frequency and a 5% power loss is feasible, with an inductance of 1.569 μH and a resistance of 3.45 $m\Omega$. Though adding a magnetic material increases the inductance, it also increases the costs of the integration. In the future the operating frequencies of PV boost converters is expected to increase, allowing for lower desired inductance values [71].

One way of decreasing the resistance of the coil would be by using a Litz wire. A Litz wire is a multi-strand wire which is designed to reduce both the skin and proximity effect losses in conductors up to frequencies of hundreds of kHz [72]. This implies that the resistance in a Litz wire will be lower than the simulated copper wire used in this research. Further analysis on Litz wires for the integration onto c-Si solar cells would have to be done, to see if this type of wire is possible for solar cell integration, by for instance screen printing. However, as stated earlier, this research focuses on a specific case where a copper wire is used.

5.3. Multiple coils per cell

As stated in Section 3.2, increasing the series resistance of a solar cell decreases the fill factor, and thus we want to create a planar inductor with an as low as possible series resistance. However, from the previous section, it became clear that there are just three ($M = 1, 2, 3$) coils that have a resistance below the threshold. One possible way to lower high resistance values would be by integrating multiple coils on a single cell, as can be seen in Figure 5.4.

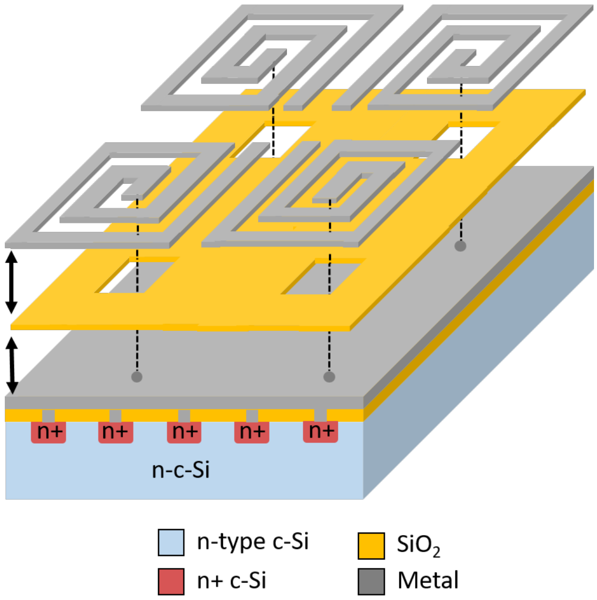

Figure 5.4: Decoupled approach with 4 coils on a single FBC solar cell.

The case shown above indicates a parallel connection between all the coils on the cell, which would result in a decrease in resistance, thus a decrease in power loss [73]. The decrease in power loss comes from Equation (5.1) [74]:

$$P_{loss} = R \cdot I^2 = \rho \frac{L}{A} \cdot I^2 \tag{5.1}$$

With the current I through the coil, and where the resistance R is calculated with the resistivity ρ, the length L, and cross-sectional area A of the conductor. When increasing the number of turns on a cell M times, the resistance also increases M times. However, the current gets divided M times, and since the power loss depends on the current squared, the power loss decreases with the increasing number of turns. This can be seen for a 4, 6, and 8-turn coil in Table 5.4, where with the increasing number of coils, the resistance decreases.

Table 5.4: The resistance for a 4, 6, and 8-turn coil ($s = 500\mu m$, $t = 200\mu m$) and the power loss for an entire cell with varying numbers of coils per cell (M).

M	4 turns		6 turns		8 turns	
	$\mathbf{R}_{coil}$ $(m\Omega)$	$\mathbf{P}_{loss,cell}$ (mW)	$\mathbf{R}_{coil}$ $(m\Omega)$	$\mathbf{P}_{loss,cell}$ (mW)	$\mathbf{R}_{coil}$ $(m\Omega)$	$\mathbf{P}_{loss,cell}$ (mW)
1	6.171	6.171	13.715	13.715	24.406	24.406
4	6.436	1.609	14.538	3.635	26.380	6.595
9	6.717	0.746	15.437	1.715	28.675	3.186
16	7.020	0.439	16.469	1.029	31.325	1.958

The table shows that increasing the number of coils per cell M times results in a power loss decrease of $\sim M$. Though it was expected that this would occur given Equation (5.1), the model confirms the method, thus allowing for further research of this approach. One setback of this approach however would be the decrease in inductance as well due to the parallel connection, as is shown in Equation (5.2) [75]:

$$\frac{1}{L} = \frac{1}{L_1} + \frac{1}{L_2} + \frac{1}{L_3} + \cdots + \frac{1}{L_N} \tag{5.2}$$

The inductance values for the coil and the cell for varying turns (4, 6, and 8) are shown in Table 5.5:

Table 5.5: The inductance for a 4, 6, and 8 turn coil ($s = 500\mu m$, $t = 200\mu m$) and a cell with M coils.

	4 turns		**6 turns**		**8 turns**	
M	$\mathbf{L}_{coil}$ (μH)	$\mathbf{L}_{cell}$ (μH)	$\mathbf{L}_{coil}$ (μH)	$\mathbf{L}_{cell}$ (μH)	$\mathbf{L}_{coil}$ (μH)	$\mathbf{L}_{cell}$ (μH)
1	0.923	0.923	2,029	2,029	3.558	3.558
4	0.467	0.117	1,024	0,256	1.796	0.449
9	0.315	0.035	0,689	0,077	1.210	0.134
16	0.239	0.015	0,521	0,033	0.916	0.057

When looking at both Table 5.4 and Table 5.5, a trade-off has to be made between the power loss and the inductance, since both decrease with an increasing number of coils per cell. The following graphs can be extracted, where in Figure 5.5 the inductance is plotted for the different coils per cell with the different thresholds for the varying frequencies. In Figure 5.6 the resistance values for the different coils per cell are shown, with the maximum allowed added series resistance for a 1%, 3%, and 5% power loss.

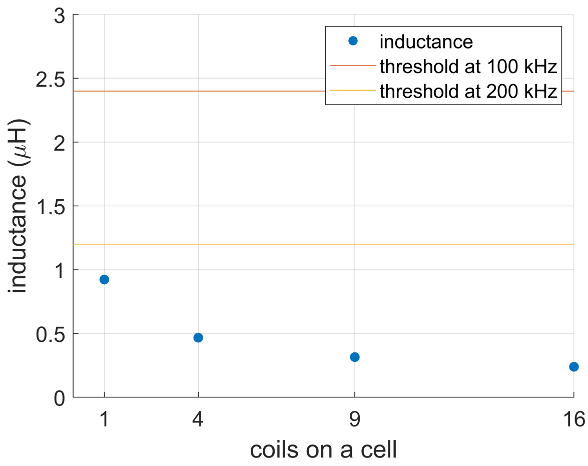

(a) 4 turns

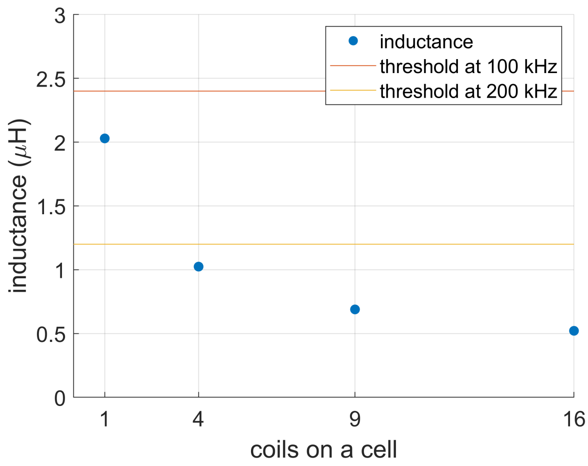

(b) 6 turns

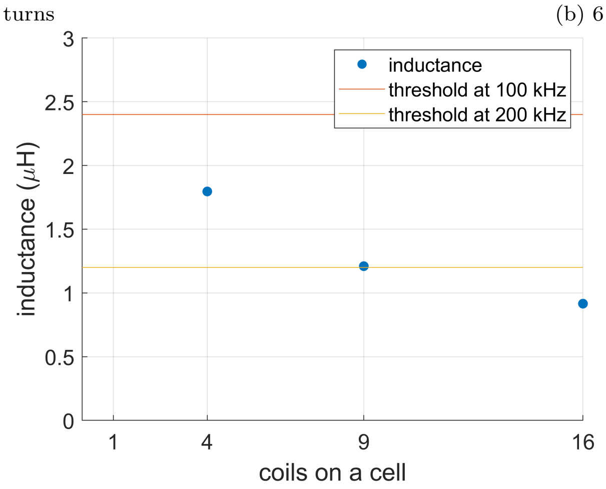

(c) 8 turns

Figure 5.5: Inductance versus the number of coils on a cell for 4, 6, and 8-turn coils.

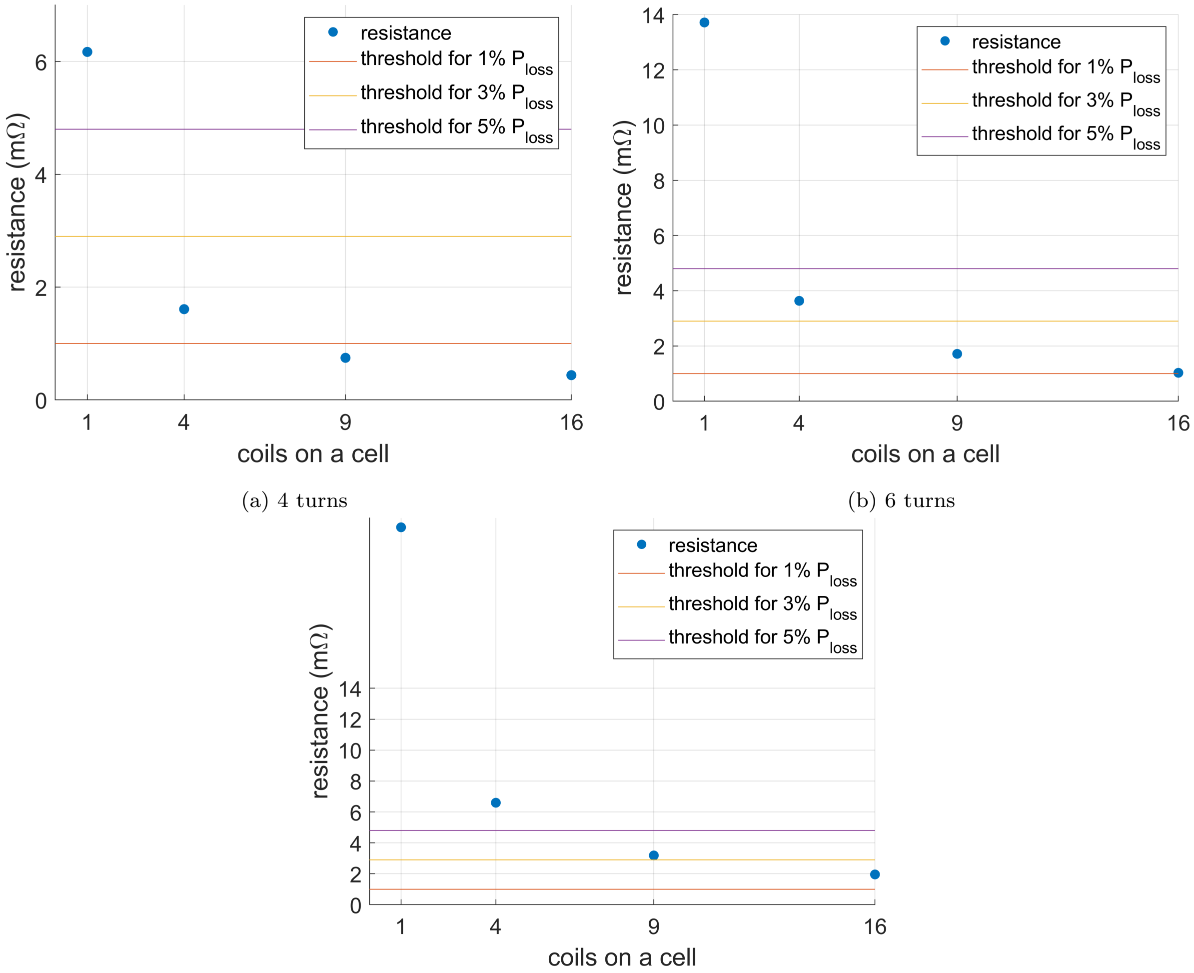

(a) 4 turns

(b) 6 turns

(b) 8 turns

Figure 5.6: Resistance versus the number of coils on a cell for 4, 6, and 8-turn coils.

For the 4-turn coil, there is no number of coils that fit within the range of inductance and resistance. This is mainly due to the low inductance values obtained by the 4-turn coil. However, when adding a magnetic material, as discussed in Section 4.9, the inductance could be increased by 200% in the sandwich structure. With an inductance value of $0.467\mu H$ for the 4 coil topology, in case of an added magnetic material, this could be increased up to $1.401\mu H$, reaching the inductance threshold for a 200 kHz frequency. The resistance for this topology is already below both the 5% and 3% thresholds. The 9 and 16 coils per cell topologies will not reach high enough inductance values, even when adding a magnetic material.

For the 6-turn coil, the same problem arises as for the 4-turn coil, where there is no number of coils per cell that are in the inductance and resistance range. For this case, the 4 coils per cell are much closer to the inductance threshold, while maintaining a resistance value below the 5% threshold. The same would apply here as for the 4-turn coil, where adding a magnetic material can increase the inductance, thus creating a feasible option for the integration onto a c-Si solar cell. Studying the 9 and 16 coils per cell topologies, both are below the 3% threshold for the resistance but do not reach high enough inductance values. In the case where adding a sandwich structure magnetic material would increase the inductance by 200%, both the 9 and 16 coils topologies will exceed the inductance threshold, creating feasible options. Their resistance values are 1.70 $m\Omega$ and 1.03 $m\Omega$, and inductance values 2.067 μH and 1.563 μH, respectively.

Lastly, the 8-turn coil is inspected, where there are just two topologies below the 5% resistance threshold, the 9 and 16 coils per cell. The inductance values for all but the 16 coils per cell are above the 200 kHz threshold, which indicates that the 9 coils per cell topology are already a feasible option for reaching a high enough inductance of 1.210 μH and a low enough resistance of 3.19 $m\Omega$ for c-Si solar cell integration. With the addition of a 200% inductance increasing magnetic material, the 16 coils topology will also exceed the 200 kHz inductance threshold with 2.748 μH and even falls below the 3% power loss threshold with a resistance of 1.96 $m\Omega$.

5.4. Conclusion

Initially for a single-coil onto a single cell, only the 3-turn coil with a boosted inductance falls in the region of high enough inductance and low enough resistance. The rest of the turns have either too high resistance or too lower inductance values. One way of overcoming the former is by adding more coils to a single cell, thus 4, 9, and 16 coils per cell were investigated. This increases the number of feasible options. For the 4-turn coil, when parallel connection 4 coils on a single cell, in case the inductance is boosted by 200%, this option is feasible and even falls below the 3% threshold for power loss. For the 6-turn coil, the 4, 9, and 16 coils per cell design are feasible when boosted, for which the latter two can even have a 3% power loss. Lastly, the 8-turn coil shows some promising results as well, whereas, for the 9 coils per cell, the integration would be feasible without boosting the inductance and a 5% power loss. The 16 coils per cell would only be feasible when boosting the inductance by 200%. The bottleneck of this approach is however the assumption that no inductive effects, such as skin effect, take place. It seems that this is the case, thus increasing the resistance at thicknesses lower than the skin depth. Further research into this specific model has to be done using a 3D model which takes any inductive effects into account. Also the integration of a coil or multiple coils on every cell in a module, will increase the production costs, making this option most likely not feasible for industrial implementation.

6

Screen printing thickness exceeding coil(s)

This chapter focuses on the second approach that has been looked at, which is the *screen printing thickness exceeding coil(s)* approach. This approach looks into finding an optimal planar coil design without taking the fabrication process of a c-Si solar cell into account. First, a set of assumptions for this approach is highlighted, after which the results for a single-cell and multiple-cell connections are discussed.

6.1. Assumptions

6.1.1. Thickness

For this decoupled approach, a single planar inductor is designed for a sub-module of 16 series-connected PV cells. This research assumes that the planar coil is free of the thickness limitations proposed in the *screen-printed approach* from Chapter 5. Hence the coil diameter and spacing are fixed like the *screen-printed approach*, but the thickness ranges from 10 up to 3500 μm. With a screen printing process, it is not possible to reach thicknesses of 3500 μm. For conductors with a thickness above the screen printing limit ($\pm 225 \mu m$), a different approach is needed for the implementation of such thick conductors. This would make the implementation process more complex, minimizing the possibility of integrating the planar inductor into the fabrication process of a c-Si solar cell.

6.1.2. Both models

For the modeling of this approach, both the 2D and 3D models have been used. The 2D model has been used up to a thickness of 300 μm in the Stationary Study, and the 3D model has been used from a thickness of 300 μm up to 3500 μm using the Frequency Domain study, for which the reasons have been discussed in Section 4.8.

6.2. Results

The tables for the resistance and inductance values for varying thicknesses and frequencies can be seen in Appendix C. In the following graphs, the resistance versus the number of turns for both a 400μm and a 2000μm conductor is shown.

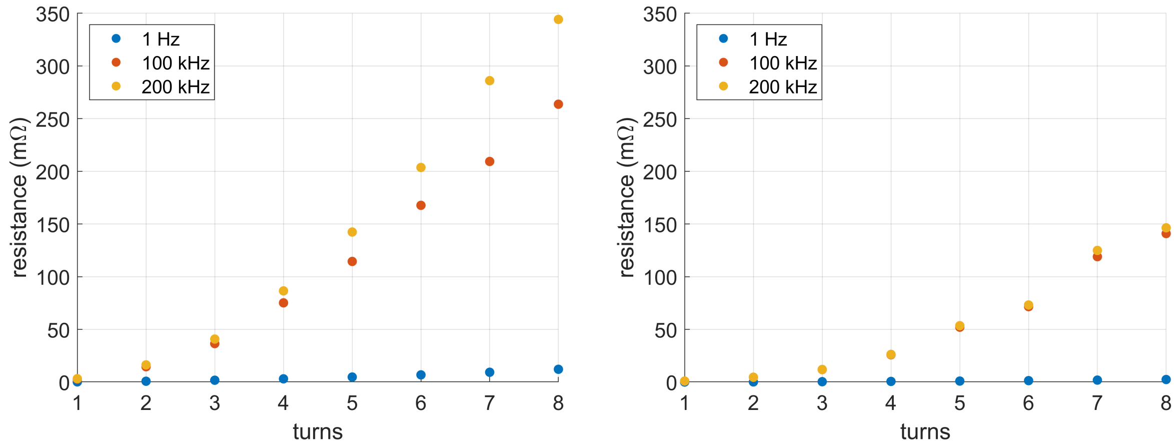

(a) 400 μm (b) 2000 μm

Figure 6.1: Resistance values for the different turns for varying frequencies and a fixed thickness of (a) 400 μm and (b) 2000 μm.

Both graphs indicate an increase in resistance with an increasing number of turns, as is expected since the total conductor length increases and the conductor width decreases. At first glance, for both thicknesses in the Frequency Domain, the resistance is too high given the maximum threshold value of $4.8 m\Omega$ for a single coil on a single cell. However, when we make a single special cell in a series connection of multiple cells, we can increase the threshold of the series resistance, as can be seen in the table below:

Table 6.1: Resistance and inductance values for series-connected cells with one special cell.

Cells per coil	**Series resistance,** 5% P_{loss} ($m\Omega$)	**Inductance,** 200 kHz (μH)
1	4.8	1.20
8	38.4	9.60
16	76.8	19.20

When for instance series connecting 16 cells with one special cell, the series resistance is increased up to an allowed value of 76.8 $m\Omega$. This would however also mean that the inductance would have to be increased up to 19.2 μH since it has to support not one, but 16 cells. For a 4, 6, and 8-turn coil the resistance and inductance values with their respective thresholds are plotted below.

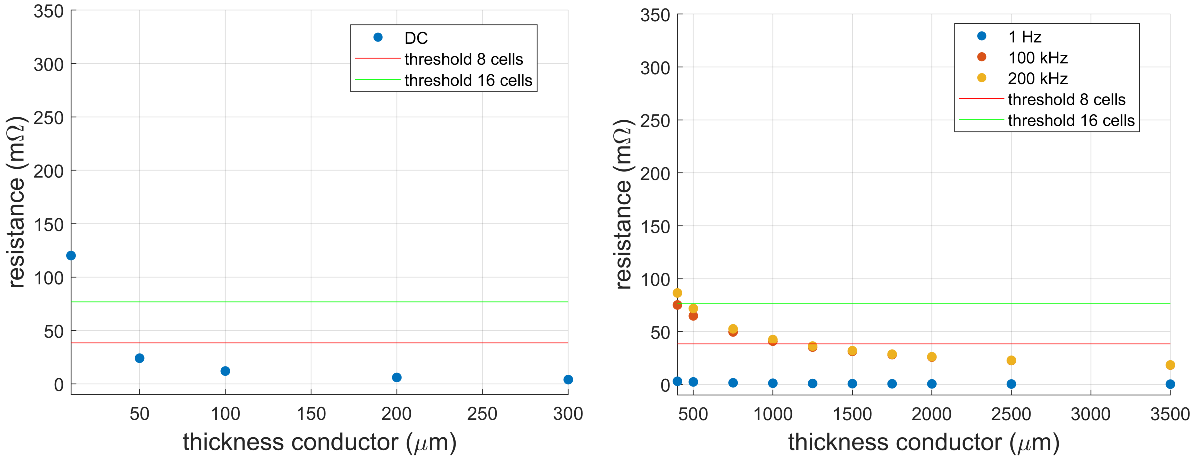

(a) (b)

Figure 6.2: Resistance versus conductor thickness for a 4-turn coil, where (a) uses the 2D model, and (b) the 3D model. The thresholds are for a 5% power loss.

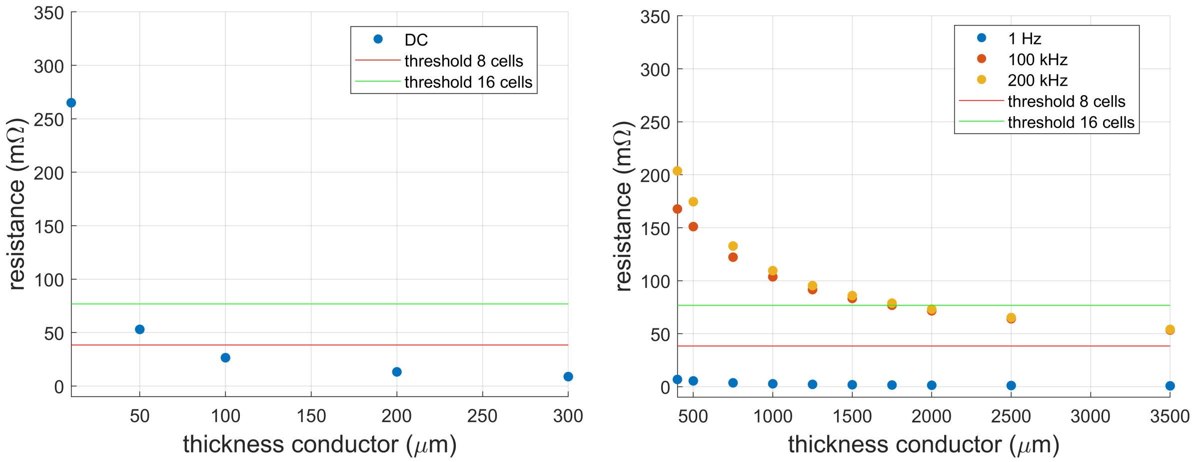

(a) (b)

Figure 6.3: Resistance versus conductor thickness for a 6-turn coil, where (a) uses the 2D model, and (b) the 3D model. The thresholds are for a 5% power loss.

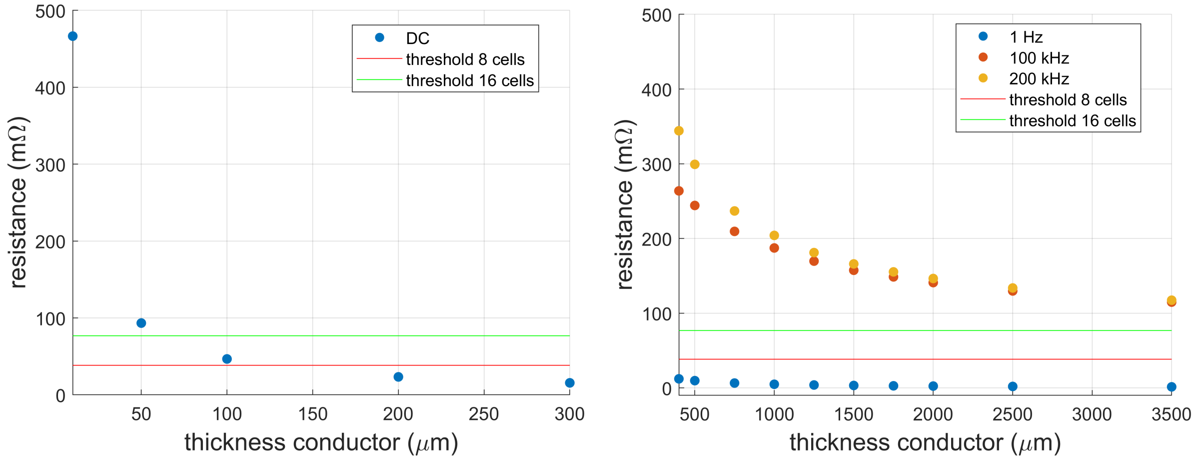

(a) (b)

Figure 6.4: Resistance versus conductor thickness for an 8-turn coil, where (a) uses the 2D model, and (b) the 3D model. The thresholds are for a 5% power loss.

Next are the inductance values for the 4, 6, and 8-turn coil shown in the range from 10 to 3500 μm.

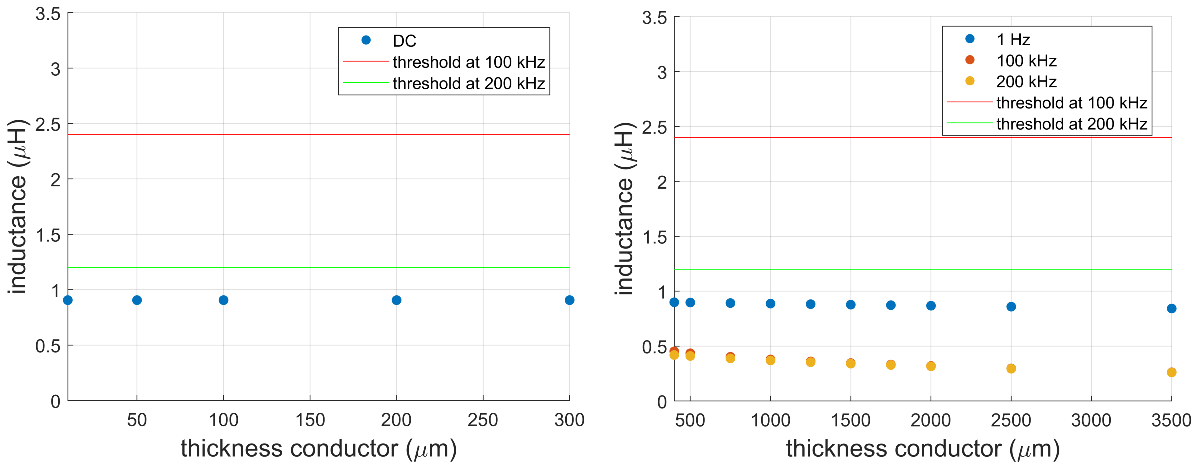

(a) (b)

Figure 6.5: Inductance versus conductor thickness for a 4-turn coil, where (a) uses the 2D model, and (b) the 3D model.

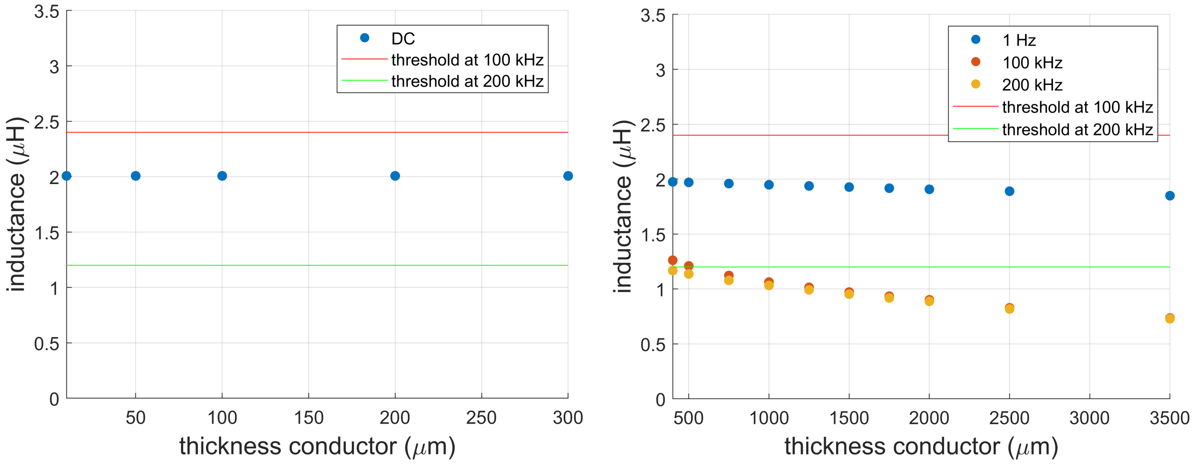

(a) (b)

Figure 6.6: Inductance versus conductor thickness for a 6-turn coil, where (a) uses the 2D model, and (b) the 3D model.

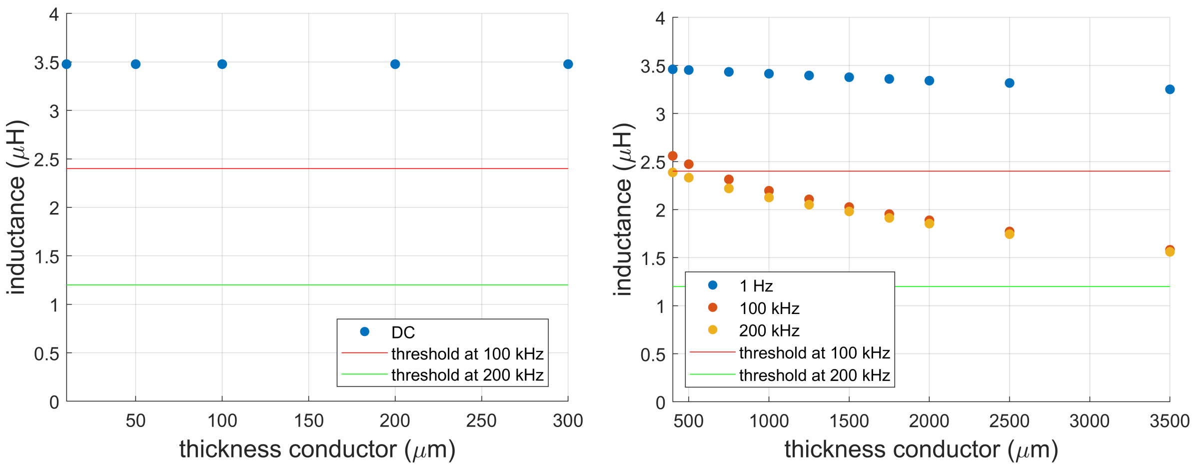

(a) (b)

Figure 6.7: Inductance versus conductor thickness for an 8-turn coil, where (a) uses the 2D model, and (b) the 3D model.

One of the first things that we notice when examining at the graphs above, is the decrease in inductance between the DC mode and the AC modes. One explanation for this behavior might be due to the distribution of magnetic flux creating currents in the conductor. Since the inductive reactance, which is the electrical resistance of an inductor in an AC system, increases with increasing frequency, Equation (6.1) shows that the inductance decreases with increasing frequency.

$$X_L = 2\pi f L \tag{6.1}$$

As can be seen between the 2D and 3D plots above, the DC inductance has less than a 0.01% percentage difference, meaning that the drop in inductance is due to the increasing frequency. What is also visible in the graphs is the decrease in inductance with increasing conductor thickness. The exception is for the DC mode, which ranges from 10 to 300 μm. An explanation could be that COMSOL calculates the inductance according to the magnetic flux in the surrounding air, and this surrounding air domain decreases with increasing conductor thickness. However, since in this model an IED is used, it is highly unlikely that an increase of the conductor from 500 μm to 3500 μm, will result in a decrease of almost 1 μH since the change in conductor thickness is negligible in comparison to the virtual infinite domain. A physical explanation is yet to be found.

An analysis of the graphs and the data from appendix C is done for a 'normal' planar coil and a 'boosted' planar coil. The boosted planar coil means a coil that has a magnetic material in a sandwich structure attached to it, which increases the inductance by 200%. This is a best-case scenario used to see what the possibilities are for solar cell integration, without taking the effects on the solar cell and the skin effect into account for a thickness up to 300μm. The quality factor for a 1 Hz, 100 kHz, and 200 kHz frequency can be seen in Appendix E.

Examining the 2D models for the 4-turn coils, the inductances are too low for both the 100 and 200 kHz thresholds for all thicknesses. However, when boosted, the inductance for a single cell for both 100 and 200 kHz is adequate, reaching values above the threshold. This is not the case for the 8 cells or the 16 cells connection, thus eliminating this option. As for the single-cell connection, for a thickness of 300 μm, the boosted inductance exceeds the thresholds (for both the 100 and 200 kHz), and the resistance falls below the thresholds, making this a solid option.

The 3D model of the 4-turn coil shows that the resistance values are below the threshold for 8 series-connected cells for both the 100 and 200 kHz from a thickness of 1250μm. When series connecting 16 cells, all the thicknesses for the 100 kHz are below the threshold and above the 500μm for the 200 kHz. However, comparing this to the inductance values, only the boosted inductance for a thickness of 400 and 500 μm are adequate for a single-cell connection. Since there is no overlapping thickness for the 3D model where the resistance and inductance values are adequate, the 4-turn coil above 300 μm is not feasible.

The 6-turn coil for a thickness of 10 to 3500 μm, only has a high enough inductance for a single-cell connection for both the 100 and 200 kHz frequency. Since the resistance values are above the threshold for a single-cell connection for any thickness, with the lowest value being 8.84 $m\Omega$ for the 2D and 53.44 $m\Omega$ for the 100 kHz 3D models, not a single combination is feasible.

As for the 8-turn coil, all thicknesses for both the 100 and 200 kHz case with the boosted inductance reach high enough inductance values for a single-cell connection. All the resistance values fall above the threshold for a single-cell connection. Only the 2D model (10 - 300 μm) has a high enough inductance, when boosted, for the 200 kHz frequency for an 8-cell connection. For thicknesses of 200 and 300 μm, the resistance falls below the threshold, giving two more feasible options.

With the statements from above, the conclusion is drawn that with the given designs, so the 4, 6, or 8-turn coil for a thickness ranging from 10 to 3500 μm for either single or multiple connected cells, just three feasible options arise: the 4-turn, single-cell connection with a thickness of 300 μm, the 8-turn, 8 cell connection with a thickness of 200 μm and the 8-turn, 8 cell connection with a thickness of 300 μm.

6.3. Conclusion

This chapter sheds light on the possibilities of implementing a coil onto a solar cell without taking the production process into account. This allows for all ranging thicknesses, and in this research, the range from 10 to 3500 μm is studied. By comparing the inductance and resistance values for a 4, 6, and 8-turn coil for either a single or multiple cell connection, several feasible values have been found. For the 4-turn coil, a single-cell connection with a thickness of 300 μm is feasible and for the 8-turn coil, when series connecting eight cells, the planar inductor reaches for the 200 and 300 μm thickness high enough inductance and low enough resistance values. For all three options, the inductance will have to be boosted by 200 %.

7
Conclusions and Discussion

In this thesis work, a model has been created using COMSOL Multiphysics® in order to investigate the feasibility of integrating a square planar inductor onto a c-Si solar cell. In this chapter the main findings of the research are summarized and used to answer the research questions stated in Section 1.6, followed by recommendations regarding future research on the integration of a planar inductor in Section 7.2.

7.1. Conclusions

The first research objective was to find the required inductance values needed for a solar cell in a DC-DC boost converter connection. For this research the *Gen 2 Cell - 160 mm* c-Si solar cell has been used, which has a V_{mpp} of 0.575V and an I_{mpp} of 5.98A. Using these two values and a virtual DC-DC boost converter with a duty cycle of 0.5 and a current ripple of 20%, for varying frequencies the needed inductance values are calculated. For 100 and 200 kHz, where the 200 kHz is an operating frequency commonly used in PV power converters, the required inductance values are 2.40 μH, and 1.20 μH, respectively. When series connecting multiple cells, the required inductance will scale linearly.

The second objective was to find the maximum allowed added series resistance when series connection a planar inductor onto a specific c-Si solar cell. Using the datasheet from the *Gen 2 Cell - 160 mm* solar cell, the IV curve has been obtained using the LTSpice software. Multiple IV curves have been plotted, each with an added series resistance to the already present series resistance of 4.3 $m\Omega$ of the solar cell. Five different power loss values have been appointed (1 to 5 % of the maximum), which corresponded to a given PV curve with a certain added series resistance. The resistance values are 1.0, 2.0, 2.9, 3.9, and 4.8 $m\Omega$ for a power loss percentage of 1, 2, 3, 4, and 5%, respectively. So all resistance values for a single cell connection should be lower than these values for the respective power loss percentages. The allowed series resistance also increases linearly with the number of increased series-connected cells.

The third objective was to research the feasibility of integrating a square planar inductor into a c-Si solar cell production process. Using COMSOL Multiphysics®, two different square planar coil models have been created; a 2D and a 3D model. The 2D model has been used to investigate conductor thicknesses ranging from 10 to 300 μm, while for higher thicknesses the 3D model has been used. A way of integrating the planar inductor is by using the screen printing technique. The advantage of this technique is the ability of implementing the integration into the production process of a c-Si solar cell, but the limitation is the achievable thickness, which ranges from 10 to 200 μm, thus only allowing for the use of the 2D model. In the best-case scenario, where skin effect is not taken into account for the 2D model, the inductance values for varying thicknesses stay equal with increasing conductor thickness. Therefore a thickness of 200 μm is chosen for this approach since this will result in the lowest resistance. For the air-core single-cell inductors for DC-DC boost converter applications, the inductance and resistance values were either below the 1.20 μH threshold or above the 4.8 $m\Omega$ threshold, respectively. However, the inductance can be increased up to 200% using a sandwich structure magnetic material. In a boosted-inductance case, the 3-turn coil with a thickness of 200 μm, and a 5% power loss is the only configuration that is feasible for a 200 kHz DC-DC boost converter application, with a reached inductance of 1.569 μH and a resistance of 3.45 $m\Omega$.

Even though the inductance can be increased using a magnetic material, for many coil configurations the resistance is still above the highest threshold value of 4.8 $m\Omega$. The series resistance can be decreased in two ways: by increasing the number of coils per cell or increasing the number of connected cells to a single coil. For the former method, there are six options that allow for solar cell integration for DC-DC boost converter applications. Nine parallel-connected 8-turn coils with a thickness of 200 μm reach an inductance of 1.210 μH and a resistance of 3.19 $m\Omega$, allowing for a 200 kHz DC-DC boost converter application without any magnetic inductance increase. The other five are only applicable for either the 100 or 200 kHz boost converter application in case of an inductance increase by adding a magnetic material. The four parallel-connected 4 and 6-turn coils with a thickness of 200 μm, reach a boosted inductance of 1.401 μH, and 3.072 μH, and a resistance of 1.61 $m\Omega$ and 3.64 $m\Omega$, respectively. The 6-turn coils in a nine and sixteen parallel connection also reach high enough inductances of 2.067 μH and 1.563 μH, and low enough resistances of 1.70 $m\Omega$ and 1.03 $m\Omega$, respectively. Lastly, the sixteen parallel-connected 8-turn coils with a thickness of 200 μm reach an inductance of 2.748 μH and a resistance of 1.96 $m\Omega$, meaning that this configuration can even operate at a frequency of 100 kHz. All of the above options would however be implemented on every single cell in a panel, making it a very expensive approach.

For the *screen printing thickness exceeding coil(s)* approach, a thickness range from 10 to 3500 μm is examined for frequencies of 100 and 200 kHz. At a frequency of 200 kHz, the skin effect is quite noticeable for higher thicknesses since the resistance values decrease more slowly with increasing thickness. As a result, only the 4-turn coil with a thickness of 300 μm, a magnetically increased inductance of 2.718 μH, and a resistance of 4.01 $m\Omega$, is feasible for the 100 and 200 kHz DC-DC boost converter applications. By connecting a single coil to multiple series-connected cells, the series resistance can be increased. Since a higher inductance would be needed too, the only feasible option for this approach is the eight-cell connected 8-turn coil for a thickness of 200 μm and 300 μm, both reaching a magnetically increased inductance of 10.431 μH and resistance of 23.33 $m\Omega$ and 15.56 $m\Omega$, respectively.

The last research objective was to see how the skin effect affects the rectangular wire for varying dimensions. By creating a straight wire in a cylindrical air domain with an IED, the skin effect was measured. By setting the thickness to 200 and 1000 μm for a width of 4 cm each, the skin effect is measured for both instances at varying frequencies. The 200 μm has been chosen, since this thickness is still smaller than twice the skin depth for a frequency of 200 kHz, and no skin effect is expected to occur. However, for both the 200 and 1000 μm conductors, there seems to be an increase in resistance at much lower frequencies than expected, where the 200 μm increases from 104.75$m\Omega$ in DC to 176.17$m\Omega$ at 200 kHz, and the 1000 μm increases from 20.951$m\Omega$ in DC to 102.51$m\Omega$ at 200 kHz. Though the percentage increase in resistance of the 1000 μm conductor is higher than that for the 200 μm conductor, the initial assumption of no skin effect at thicknesses smaller than the skin depth is incorrect, and should therefore be taken into account for the simulation.

7.2. Future Research

In this section, the recommendations for further research are presented. These recommendations are done since these options could not be explored within the time frame of this thesis project.

Firstly, the geometrical shape of the planar coil has to be further investigated. In this research, a square shape has been used, since literature showed that several square planar inductors have higher inductance values than other shapes, and due to the possible ease of integration onto a c-Si solar cell. However, it is shown that a large bottleneck of the results is the resistance, which could be decreased by changing the shape into for instance hexagonal, or circular.

Secondly, the filling of the area might have some impact on the inductance. In this research, the entire area of the solar cell is filled with the planar coil in order to minimize resistive losses. However, when increasing the inner diameter of the planar coil, the inductance can be increased. This would however mean that the model will have to be redesigned, which was not possible with the current parameterized model. Though this would increase the resistance for the same number of turns, it could be possible to achieve a coil with a better quality factor.

Thirdly, the copper wire used for this research shows rather high resistance values for high frequencies due to the skin effect. This resistance could be minimized using a Litz wire, though the integration of the Litz wire has to be investigated.

References

[1] Rebecca Lindsey. "Climate Change: Atmospheric Carbon Dioxide". In: *Climate.gov* (2020). URL: https://www.climate.gov/news-features/understanding-climate/climate-change-atmospheric-carbon-dioxide#.

[2] United Nations. *2021 joins top 7 warmest years on record: WMO*. 2022. URL: https://news.un.org/en/story/2022/01/1110022.

[3] Max Roser Hannah Ritchie and Pablo Rosado. "CO and Greenhouse Gas Emissions". In: *Our World in Data* (2020). https://ourworldindata.org/co2-and-other-greenhouse-gas-emissions.

[4] O. Edenhofer et al. *Climate Change 2014: Mitigation of Climate Change. Contribution of Working Group III to the Fifth Assessment Report of the Intergovernmental Panel on Climate Change*. Cambridge, United Kingdom: Cambridge University Press, 2014.

[5] N S Lewis et al. "Basic Research Needs for Solar Energy Utilization. Report of the Basic Energy Sciences Workshop on Solar Energy Utilization, April 18-21, 2005". In: (Apr. 2005). URL: https://www.osti.gov/biblio/899136.

[6] IEA. *Solar PV*. Nov. 2021. URL: https://www.iea.org/reports/solar-pv.

[7] Our World in Data. *Installed solar energy capacity*. 2021. URL: https://ourworldindata.org/grapher/installed-solar-pv-capacity?time=2000..latest%5C&country=~OWID_WRL.

[8] International Renewable Energy Agency. *Solar Power*. 2020. URL: https://www.irena.org/costs/Power-Generation-Costs/Solar-Power.

[9] Christophe Ballif et al. "Status and perspectives of crystalline silicon photovoltaics in research and industry". In: *Nature Reviews Materials* (2022). ISSN: 20588437. DOI: 10.1038/S41578-022-00423-2.

[10] Fraunhofer ISE. "Photovoltaics report". In: (2021). URL: https://www.ise.fraunhofer.de/en/publications/studies/photovoltaics-report.html.

[11] TNO. *Back Contact Solar Panels: Combining High Power and Aesthetics*. URL: https://www.tno.nl/en/focus-areas/energy-transition/roadmaps/renewable-electricity/solar-energy/solar-panel-efficiency/back-contact-solar/.

[12] D Van Nijen et al. *Exploring the benefits, challenges, feasibility and progress of integrating power electronics into c-Si solar cells*. 2022.

[13] A.H.M. Smets et al. *Solar Energy: The Physics and Engineering of Photovoltaic Conversion, Technologies and Systems*. UIT Cambridge, 2016. ISBN: 9781906860325.

[14] Mohd Zulkifli Ramli and Zainal Salam. "Performance evaluation of dc power optimizer (DCPO) for photovoltaic (PV) system during partial shading". In: *Renewable Energy* 139 (Aug. 2019), pp. 1336–1354. ISSN: 18790682.

[15] Shifeng Deng et al. "Research on hot spot risk for high-efficiency solar module". In: *Energy Procedia* 130 (2017), pp. 77–86.

[16] Hesan Ziar, Patrizio Manganiello, and Miro Zeman. "Photovoltatronics: intelligent PV-based devices for energy and information applications". In: *This journal is Cite this: Energy Environ. Sci* 14 (2021), p. 106. DOI: 10.1039/d0ee02491k.

[17] PV Education. *Shunt Resistance*. URL: https://www.pveducation.org/pvcdrom/solar-cell-operation/shunt-resistance.

[18] O. Breitenstein et al. "Localization of shunts across the floating junction of DSBC solar cells by lock-in thermography". In: Feb. 2000, pp. 124–127.

[19] PV Education. *Series Resistance*. URL: https://www.pveducation.org/pvcdrom/solar-cell-operation/series-resistance.

[20] Marco Rosa-Clot and Giuseppe Marco Tina. "Introduction to PV Plants". In: *Submerged and Floating Photovoltaic Systems* (Jan. 2018), pp. 33–64.

[21] Ned Mohan, Tore M. Undeland, and William P. Robbins. *Power Electronics*. Second. John Wiley & Sons, Inc., 1995.

[22] Jih-Sheng Jason Lai and Douglas J. Nelson. "Energy Management Power Converters in Hybrid Electric and Fuel Cell Vehicles". In: *Proceedings of the IEEE* 95 (2007), pp. 766–777.

[23] NASA. *Our Sun*. URL: `https://solarsystem.nasa.gov/solar-system/sun/in-depth/`.

[24] Office of Energy Efficiency & Renewable Energy. *How Does Solar Work?* URL: `https://www.energy.gov/eere/solar/how-does-solar-work`.

[25] ACS. *Energy from the Sun*. URL: `https://www.acs.org/content/acs/en/climatescience/energybalance/energyfromsun.html`.

[26] Simon Philipps. "Photovoltaics Report". In: (July 2021). URL: `https://www.ise.fraunhofer.de/en/publications/studies/photovoltaics-report.html`.

[27] PV Education. *Short-Circuit Current*. URL: `https://www.pveducation.org/pvcdrom/solar-cell-operation/short-circuit-current`.

[28] M. Padilla et al. "Short-circuit current density mapping for solar cells". In: *Solar Energy Materials and Solar Cells* 120 (PART A 2014), pp. 282–288. ISSN: 09270248. DOI: `10.1016/j.solmat.2013.09.019`.

[29] Hitoshi Sai, Hiroshi Umishio, and Takuya Matsui. "Very Thin (56 m) Silicon Heterojunction Solar Cells with an Efficiency of 23.3% and an Open-Circuit Voltage of 754 mV". In: *Solar RRL* 5 (11 Nov. 2021).

[30] PV Education. *Open-Circuit Voltage*. URL: `https://www.pveducation.org/pvcdrom/solar-cell-operation/open-circuit-voltage`.

[31] Michelle Farnum. *What is an Inductor?* 2020. URL: `https://www.cettechnology.com/what-is-an-inductor/`.

[32] Mark Harris. *Inside Pascal: NVIDIA's Newest Computing Platform*. 2016. URL: `https://developer.nvidia.com/blog/inside-pascal/`.

[33] S. M. Sze. *Semiconductor devices - physics and technology*. Vol. 2. Wiley, 2002. ISBN: 0471333727.

[34] Yasushi Katayama et al. "High-power-density MHz-switching monolithic DC-DC converter with thin-film inductor". In: *PESC Record - IEEE Annual Power Electronics Specialists Conference* 3 (2000), pp. 1485–1490.

[35] Alberto L. *An Overview of On-chip Inductors for Integrated Circuits IC. Types, pro & cons*. 2020. URL: `https://miscircuitos.com/an-overview-of-on-chip-inductors-for-integrated-circuits-ic-types-pro-cons/`.

[36] S. S. Mohan et al. "Simple accurate expressions for planar spiral inductances". In: *IEEE Journal of Solid-State Circuits* 34 (1999), pp. 1419–1424.

[37] Monica Zolog, Dan Pitica, and Ovidiu Pop. "Characterization of Spiral Planar Inductors Built on Printed Circuit Boards". In: *2007 30th International Spring Seminar on Electronics Technology (ISSE)* (2007), pp. 308–313. DOI: `10.1109/ISSE.2007.4432869`.

[38] Pui-Weng Chan and Syafrudin Masri. *DC-DC Boost Converter with Constant Output Voltage for Grid Connected Photovoltaic Application System*.

[39] Razman Ayop and Chee Wei Tan. "Design of boost converter based on maximum power point resistance for photovoltaic applications". In: *Solar Energy* 160 (2018), pp. 322–335. ISSN: 0038-092X. DOI: `https://doi.org/10.1016/j.solener.2017.12.016`. URL: `https://www.sciencedirect.com/science/article/pii/S0038092X17310885`.

[40] Peter Jen-Hung Huang to. *Integrating DC/DC Conversion with Possible Reconfiguration within Submodule Solar Photovoltaic Systems*. 2017.

[41] Karin Schneider, M A | Communications, and Andreas Hensel|. *Fraunhofer ISE develops highly compact inverter for direct connection to medium-voltage grid*. URL: `www.ise.fraunhofer.de`.

[42] Saleh Babaa et al. "Overview of Boost Converters for Photovoltaic Systems". In: *Journal of Power and Energy Engineering* 06 (Jan. 2018), pp. 16–31. DOI: 10.4236/jpee.2018.64002.

[43] Brigitte Hauke. "Basic Calculation of a Boost Converter's Power Stage". In: (2014).

[44] Cathy. *What Is Ripple Current In Inductor?* URL: https://somsubhra.com/what-is-ripple-current-in-inductor/.

[45] "Design of a new electrical model of a ferromagnetic planar inductor for its integration in a micro-converter". In: *Mathematical and Computer Modelling* 57 (1-2 Jan. 2013), pp. 200–227.

[46] Minh Huy Nguyen and Handy Fortin Blanchette. "Optimizing ac resistance of solid PCB winding". In: *Electronics (Switzerland)* 9 (5 May 2020).

[47] Ronan Meere et al. "Magnetic-Core and Air-Core Inductors on Silicon: A Performance Comparison up to 100 MHz". In: *IEEE Transactions on Magnetics* 47 (10 2011).

[48] Stan Zurek. *Proximity effect.* 2022. URL: https://e-magnetica.pl/proximity_effect.

[49] Alexander Anthon, Zhe Zhang, and Michael A.E. Andersen. "A high power boost converter for PV Systems operating up to 300 kHz using SiC devices". In: *Proceedings - 2014 International Power Electronics and Application Conference and Exposition, IEEE PEAC 2014* (Feb. 2014), pp. 302–307. DOI: 10.1109/PEAC.2014.7037872.

[50] Donald Gardner et al. "Integrated on-chip inductors using magnetic material (invited)". In: *Journal of Applied Physics* 103 (Apr. 2008), 07E927–07E927. DOI: 10.1063/1.2838012.

[51] Waseem A Roshen. "Analysis of Planar Sandwich Inductors by Current Images". In: *IEEE TRANSACTIONS ON MAGNETICS* 26 (1990).

[52] Walter Frei. *Computing the Inductance of a Straight Wire.* 2013. URL: https://www.comsol.com/blogs/computing-the-inductance-of-a-wire/.

[53] Han Cui et al. "Inductor Geometry With Improved Energy Density". In: *IEEE TRANSACTIONS ON POWER ELECTRONICS* 29 (10 2014). DOI: 10.1109/TPEL.2013.2289926. URL: http://ieeexplore.ieee.org..

[54] COMSOL Multiphysics. *Infinite Element Domain.* URL: https://doc.comsol.com/5.5/doc/com.comsol.help.comsol/comsol_ref_definitions.12.116.html.

[55] Friedrich Maier. *Efficient Parameter Control and Usage in COMSOL Multiphysics®.* URL: https://www.comsol.com/blogs/efficient-parameter-control-and-usage-in-comsol-multiphysics/.

[56] Magnus Ringh. *Using the Material Libraries in COMSOL Multiphysics®.* updated on 01-04-2022. 2020. URL: https://www.comsol.com/blogs/using-the-material-libraries-in-comsol-multiphysics/.

[57] COMSOL Multiphysics. *The Magnetic Fields Interface.* URL: https://doc.comsol.com/5.5/doc/com.comsol.help.comsol/comsol_ref_acdc.17.67.html.

[58] COMSOL Multiphysics. *The Electric Currents in Shells Interface.* URL: https://doc.comsol.com/5.5/doc/com.comsol.help.acdc/acdc_ug_electric_fields.07.066.html.

[59] Andrew Griesmer. *Size Parameters for Free Tetrahedral Meshing in COMSOL Multiphysics.* URL: https://www.comsol.com/blogs/size-parameters-free-tetrahedral-meshing-comsol-multiphysics/.

[60] COMSOL Multiphysics. *Stationary.* URL: https://doc.comsol.com/5.5/doc/com.comsol.help.comsol/comsol_ref_solver.27.015.html#1432247.

[61] COMSOL Multiphysics. *Frequency Domain Study.* URL: https://doc.comsol.com/5.5/doc/com.comsol.help.aco/aco_ug_study_types.15.04.html.

[62] Sunniva Tech. *SunPower Cell Pricing - specifically for small orders.* 2019.

[63] Vincenzo Stornelli et al. "A New Simplified Five-Parameter Estimation Method for Single-Diode Model of Photovoltaic Panels". In: *Energies* 12.22 (2019). ISSN: 1996-1073. URL: https://www.mdpi.com/1996-1073/12/22/4271.

[64] Donald S Gardner, Gerhard Schrom, and Peter Hazucha. "Integrated on-chip inductors using magnetic material". In: *J. Appl. Phys* 103 (2008), pp. 7–927. DOI: 10.1063/1.2838012. URL: https://doi.org/10.1063/1.2838012.

[65] Nicolas Garraud et al. "Flexible screen-printed coils for wireless power transfer using low-frequency magnetic fields You may also like Modeling and experimental analysis of rotating magnet receivers for electrodynamic wireless power transmission". In: (2019). DOI: 10.1088/1361-6439/ab26ff. URL: https://doi.org/10.1088/1361-6439/ab26ff.

[66] N J Grabham et al. "Fabrication Techniques for Manufacturing Flexible Coils on Textiles for Inductive Power Transfer". In: *IEEE Sensors Journal* 18 (6 2018), p. 2599. DOI: 10.1109/JSEN.2018.2796138.

[67] Jurica Kundrata and Adrijan Baric. "Design of a planar inductor for DC-DC converter on flexible foil applications". In: *2012 Proceedings of the 35th International Convention MIPRO* (2012), pp. 54–59.

[68] Yi Li et al. "Textile-Based Flexible Coils for Wireless Inductive Power Transmission". In: *Applied Sciences* 8.6 (2018). ISSN: 2076-3417. DOI: 10.3390/app8060912. URL: https://www.mdpi.com/2076-3417/8/6/912.

[69] Aminy E Ostfeld et al. "Screen printed passive components for flexible power electronics". In: *Nature Publishing Group* (2015). DOI: 10.1038/srep15959. URL: www.nature.com/scientificreports.

[70] Copprint. *CONDUCTIVE NANO COPPER INKS - Print Ready, Nano Copper Conductive Inks*. URL: https://www.copprint.com/products/.

[71] Christian Schöner. *GaN-resonant – Efficient, Highly Compact High-Frequency Power Electronics with GaN Transistors*. URL: https://www.ise.fraunhofer.de/en/research-projects/gan-resonant.html.

[72] Charles R. Sullivan and Richard Y. Zhang. "Simplified design method for Litz wire". In: *Conference Proceedings - IEEE Applied Power Electronics Conference and Exposition - APEC* (2014), pp. 2667–2674. DOI: 10.1109/APEC.2014.6803681.

[73] Waseem A Roshen. "Analysis of Planar Sandwich Inductors by Current Images". In: *IEEE TRANSACTIONS ON MAGNETICS* 26 (1990). DOI: 10.1109/20.104901.

[74] R. Barlik et al. "Estimation of power losses in a high-frequency planar transformer using a thermal camera". In: *Archives of Electrical Engineering* 65 (Sept. 2016). DOI: 10.1515/aee-2016-0044.

[75] All About Circuits. *Series and Parallel Inductors*. URL: https://www.allaboutcircuits.com/textbook/direct-current/chpt-15/series-and-parallel-inductors/.

A

Gen 2 Cell Data sheet

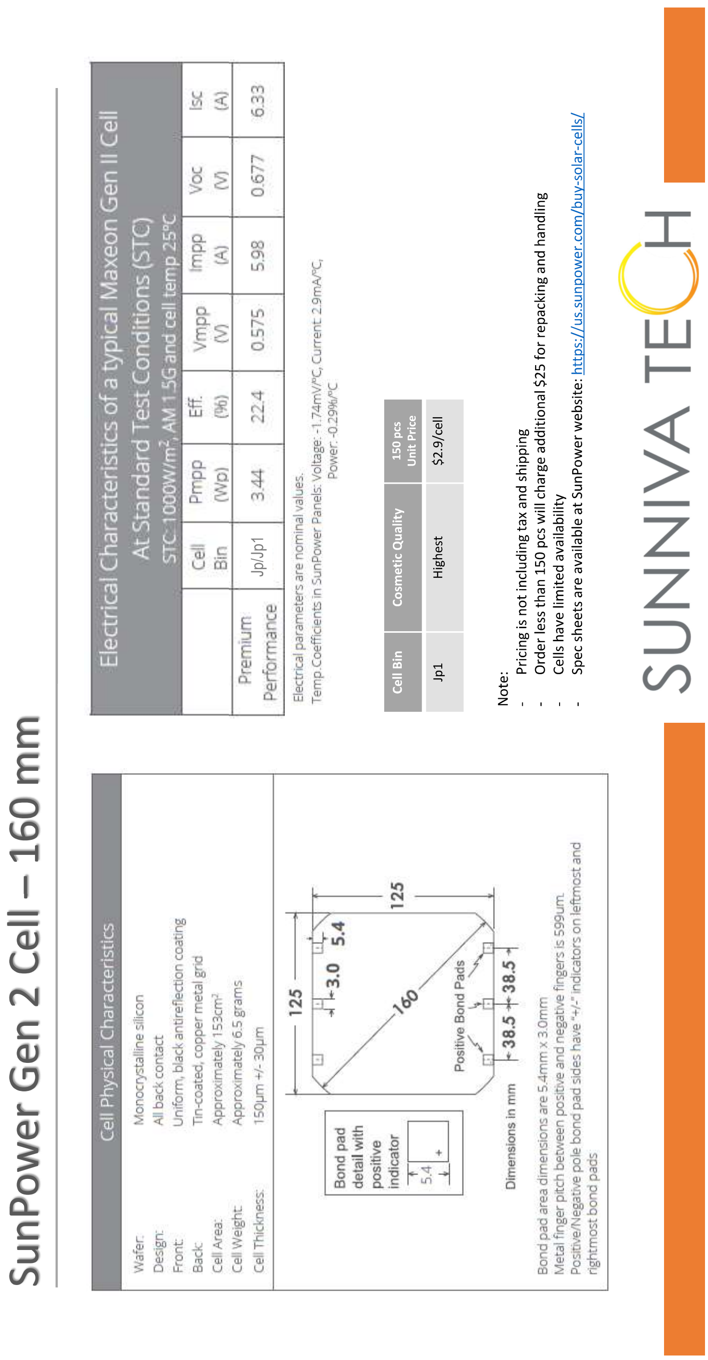

SunPower Gen 2 Cell – 160 mm

Cell Physical Characteristics	
Wafer:	Monocrystalline silicon
Design:	All back contact
Front:	Uniform, black antireflection coating
Back:	Tin-coated, copper metal grid
Cell Area:	Approximately 153cm²
Cell Weight:	Approximately 6.5 grams
Cell Thickness:	150μm +/- 30μm

Bond pad area dimensions are 5.4mm x 3.0mm
Metal finger pitch between positive and negative fingers is 599um.
Positive/Negative pole bond pad sides have "+/-" indicators on leftmost and rightmost bond pads

Electrical Characteristics of a typical Maxeon Gen II Cell
At Standard Test Conditions (STC)
STC: 1000W/m², AM 1.5G and cell temp 25°C

	Cell Bin	Pmpp (Wp)	Eff. (%)	Vmpp (V)	Impp (A)	Voc (V)	Isc (A)
Premium Performance	Jp/Jp1	3.44	22.4	0.575	5.98	0.677	6.33

Electrical parameters are nominal values.
Temp.Coefficients in SunPower Panels: Voltage: -1.74mV/°C, Current 2.9mA/°C,
Power: -0.29%/°C

Cell Bin	Cosmetic Quality	150 pcs Unit Price
Jp1	Highest	$2.9/cell

Note:
- Pricing is not including tax and shipping
- Order less than 150 pcs will charge additional $25 for repacking and handling
- Cells have limited availability
- Spec sheets are available at SunPower website: https://us.sunpower.com/buy-solar-cells/

SUNNIVA TECH

B

Geometry table

Table B.1: Parameterization of the coil geometry for 1, 2, and 3 turns.

Row number	1 turn		2 turns		3 turns	
0	xw	yw	xw	yw	xw	yw
1	-L/2+w	height+s	-L/2+w	height+s	-L/2+w	height+s
2	-L/2+w	L/2-w	-L/2+w	L/2-w	-L/2+w	L/2-w
3	L/2-w	L/2-w	L/2-w	L/2-w	L/2-w	L/2-w
4	L/2-w	-L/2+w	L/2-w	-L/2+w	L/2-w	-L/2+w
5	L/2-w-s	-L/2+w	-L/2+2*w+s	-L/2+w	-L/2+2*w+s	-L/2+w
6	L/2-w-s	L/2-w-s	-L/2+2*w+s	L/2-2*w-s	-L/2+2*w+s	L/2-2*w-s
7	-L/2+w+s	L/2-w-s	L/2-2*w-s	L/2-2*w-s	L/2-2*w-s	L/2-2*w-s
8	-L/2+w+s	-L/2	L/2-2*w-s	-L/2+2*w+s	L/2-2*w-s	-L/2+2*w+s
9	L/2	-L/2	L/2-2*w-2*s	-L/2+2*w+s	-L/2+3*w+2*s	-L/2+2*w+s
10	L/2	L/2	L/2-2*w-2*s	L/2-2*w-2*s	-L/2+3*w+2*s	L/2-3*w-2*s
11	-L/2	L/2	-L/2+2*w+2*s	L/2-2*w-2*s	L/2-3*w-2*s	L/2-3*w-2*s
12	-L/2	height+s	-L/2+2*w+2*s	-L/2+w+s	L/2-3*w-2*s	-L/2+3*w+2*s
13			L/2-w-s	-L/2+w+s	L/2-3*w-3*s	-L/2+3*w+2*s
14			L/2-w-s	L/2-w-s	L/2-3*w-3*s	L/2-3*w-3*s
15			-L/2+w+s	L/2-w-s	-L/2+3*w+3*s	L/2-3*w-3*s
16			-L/2+w+s	-L/2	-L/2+3*w+3*s	-L/2+2*w+2*s
17			L/2	-L/2	L/2-2*w-2*s	-L/2+2*w+2*s
18			L/2	L/2	L/2-2*w-2*s	L/2-2*w-2*s
19			-L/2	L/2	-L/2+2*w+2*s	L/2-2*w-2*s
20			-L/2	height+s	-L/2+2*w+2*s	-L/2+w+s
21					L/2-w-s	-L/2+w+s
22					L/2-w-s	L/2-w-s
23					-L/2+w+s	L/2-w-s
24					-L/2+w+s	-L/2
25					L/2	-L/2
26					L/2	L/2
27					-L/2	L/2
28					-L/2	height+s

C

Resistance and inductance values

Table C.1: 1 Hz resistance values for a thickness from 10 to 2000 μm, for all number of turns with a spacing of 500μm on a 12.5 cm cell. The 2D model is used for a thickness up to 300 μm, after which the 3D model is used.

t (μm)	**N**	**R** ($m\Omega$)	**N**	**R** ($m\Omega$)	**N**	**R** ($m\Omega$)	**N**	**R** ($m\Omega$)	**N**	**R** ($m\Omega$)	**N**	**R** ($m\Omega$)	**N**	**R** ($m\Omega$)	**N**	**R** ($m\Omega$)
10	1	7.06	2	31.23	3	68.86	4	120.17	5	185.63	6	265.02	7	358.59	8	466.51
50	1	1.14	2	6.25	3	13.77	4	24.06	5	37.13	6	53.01	7	71.72	8	93.31
100	1	0.71	2	3.12	3	6.89	4	12.03	5	18.57	6	26.51	7	35.87	8	46.66
200	1	0.35	2	1.56	3	3.45	4	6.02	5	9.29	6	13.26	7	17.94	8	23.33
300	1	0.24	2	1.04	3	2.30	4	4.01	5	6.19	6	8.84	7	11.96	8	15.56
400	1	0.19	2	0.80	3	1.76	4	3.08	5	4.78	6	6.84	7	9.32	8	12.14
500	1	0.15	2	0.64	3	1.41	4	2.46	5	3.82	6	5.47	7	7.45	8	9.71
750	1	0.10	2	0.43	3	0.94	4	1.64	5	2.55	6	3.65	7	4.97	8	6.47
1000	1	0.07	2	0.32	3	0.70	4	1.23	5	1.91	6	2.74	7	3.73	8	4.86
1250	1	0.06	2	0.26	3	0.56	4	0.99	5	1.53	6	2.19	7	2.98	8	3.89
1500	1	0.05	2	0.21	3	0.47	4	0.82	5	1.28	6	1.83	7	2.49	8	3.24
1750	1	0.04	2	0.18	3	0.40	4	0.71	5	1.09	6	1.57	7	2.13	8	2.78
2000	1	0.04	2	0.16	3	0.35	4	0.62	5	0.96	6	1.37	7	1.87	8	2.43

Table C.2: 1 Hz inductance values for a thickness from 10 to 2000 μm, for all number of turns with a spacing of 500μm on a 12.5 cm cell. The 2D model is used for a thickness up to 300 μm, after which the 3D model is used.

t (μm)	**N**	**L** (μH)	**N**	**L** (μH)	**N**	**L** (μH)	**N**	**L** (μH)	**N**	**L** (μH)	**N**	**L** (μH)	**N**	**L** (μH)	**N**	**L** (μH)
10	1	0.056	2	0.236	3	0.523	4	0.916	5	1.414	6	2.017	7	2.725	8	3.537
50	1	0.056	2	0.236	3	0.523	4	0.916	5	1.414	6	2.017	7	2.725	8	3.537
100	1	0.056	2	0.236	3	0.523	4	0.916	5	1.414	6	2.017	7	2.725	8	3.537
200	1	0.056	2	0.236	3	0.523	4	0.916	5	1.414	6	2.017	7	2.725	8	3.537
300	1	0.056	2	0.236	3	0.523	4	0.916	5	1.414	6	2.017	7	2.725	8	3.537
400	1	0.056	2	0.233	3	0.512	4	0.899	5	1.388	6	1.975	7	2.672	8	3.460
500	1	0.056	2	0.232	3	0.511	4	0.897	5	1.384	6	1.971	7	2.666	8	3.452
750	1	0.055	2	0.231	3	0.508	4	0.892	5	1.376	6	1.960	7	2.651	8	3.433
1000	1	0.055	2	0.230	3	0.505	4	0.887	5	1.369	6	1.949	7	2.636	8	3.414
1250	1	0.055	2	0.228	3	0.502	4	0.882	5	1.361	6	1.938	7	2.622	8	3.395
1500	1	0.055	2	0.227	3	0.500	4	0.878	5	1.354	6	1.928	7	2.607	8	3.378
1750	1	0.054	2	0.226	3	0.497	4	0.873	5	1.346	6	1.917	7	2.593	8	3.360
2000	1	0.054	2	0.225	3	0.494	4	0.868	5	1.339	6	1.908	7	2.580	8	3.342

Table C.3: 100 kHz resistance values for a thickness from 10 to 2000 μm, for all number of turns with a spacing of 500μm on a 12.5 cm cell. The 2D model is used for a thickness up to 300 μm, after which the 3D model is used.

t (μm)	**N**	**R** ($m\Omega$)	**N**	**R** ($m\Omega$)	**N**	**R** ($m\Omega$)	**N**	**R** ($m\Omega$)	**N**	**R** ($m\Omega$)	**N**	**R** ($m\Omega$)	**N**	**R** ($m\Omega$)	**N**	**R** ($m\Omega$)
10	1	7.06	2	31.23	3	68.86	4	120.17	5	185.63	6	265.02	7	358.59	8	466.51
50	1	1.14	2	6.25	3	13.77	4	24.06	5	37.13	6	53.01	7	71.72	8	93.31
100	1	0.71	2	3.12	3	6.89	4	12.03	5	18.57	6	26.51	7	35.87	8	46.66
200	1	0.35	2	1.56	3	3.45	4	6.02	5	9.29	6	13.26	7	17.94	8	23.33
300	1	0.24	2	1.04	3	2.30	4	4.01	5	6.19	6	8.84	7	11.96	8	15.56
400	1	2.75	2	14.55	3	36.50	4	75.18	5	114.46	6	167.72	7	209.35	8	263.69
500	1	2.44	2	12.73	3	31.47	4	64.85	5	104.23	6	151.08	7	196.43	8	244.17
750	1	1.88	2	9.49	3	23.50	4	49.66	5	86.16	6	122.24	7	172.94	8	209.47
1000	1	1.52	2	7.64	3	18.98	4	40.97	5	74.24	6	103.69	7	154.65	8	187.28
1250	1	1.30	2	6.48	3	16.27	4	35.37	5	66.14	6	91.62	7	141.96	8	169.67
1500	1	1.15	2	5.67	3	14.38	4	31.32	5	60.10	6	83.30	7	131.76	8	157.44
1750	1	1.03	2	5.03	3	13.02	4	28.24	5	55.69	6	76.87	7	125.23	8	148.58
2000	1	0.94	2	4.53	3	11.86	4	25.92	5	52.11	6	71.59	7	119.01	8	140.93

Table C.4: 100 kHz inductance values for a thickness from 10 to 2000 μm, for all number of turns with a spacing of 500μm on a 12.5 cm cell. The 2D model is used for a thickness up to 300 μm, after which the 3D model is used.

t (μm)	**N**	**L** (μH)	**N**	**L** (μH)	**N**	**L** (μH)	**N**	**L** (μH)	**N**	**L** (μH)	**N**	**L** (μH)	**N**	**L** (μH)	**N**	**L** (μH)
10	1	0.056	2	0.236	3	0.523	4	0.916	5	1.414	6	2.017	7	2.725	8	3.537
50	1	0.056	2	0.236	3	0.523	4	0.916	5	1.414	6	2.017	7	2.725	8	3.537
100	1	0.056	2	0.236	3	0.523	4	0.916	5	1.414	6	2.017	7	2.725	8	3.537
200	1	0.056	2	0.236	3	0.523	4	0.916	5	1.414	6	2.017	7	2.725	8	3.537
300	1	0.056	2	0.236	3	0.523	4	0.916	5	1.414	6	2.017	7	2.725	8	3.537
400	1	0.017	2	0.078	3	0.222	4	0.453	5	0.856	6	1.262	7	1.928	8	2.559
500	1	0.016	2	0.073	3	0.213	4	0.435	5	0.820	6	1.210	7	1.858	8	2.473
750	1	0.015	2	0.068	3	0.199	4	0.403	5	0.756	6	1.123	7	1.728	8	2.314
1000	1	0.013	2	0.064	3	0.188	4	0.379	5	0.712	6	1.063	7	1.636	8	2.196
1250	1	0.012	2	0.061	3	0.178	4	0.361	5	0.677	6	1.015	7	1.561	8	2.107
1500	1	0.012	2	0.058	3	0.170	4	0.346	5	0.647	6	0.972	7	1.498	8	2.027
1750	1	0.011	2	0.055	3	0.162	4	0.332	5	0.620	6	0.934	7	1.438	8	1.953
2000	1	0.010	2	0.053	3	0.156	4	0.320	5	0.596	6	0.901	7	1.387	8	1.889

Table C.5: 200 kHz resistance values for a thickness from 10 to 2000 μm, for all number of turns with a spacing of 500μm on a 12.5 cm cell. The 2D model is used for a thickness up to 300 μm, after which the 3D model is used.

t (μm)	**N**	**R** ($m\Omega$)	**N**	**R** ($m\Omega$)	**N**	**R** ($m\Omega$)	**N**	**R** ($m\Omega$)	**N**	**R** ($m\Omega$)	**N**	**R** ($m\Omega$)	**N**	**R** ($m\Omega$)	**N**	**R** ($m\Omega$)
10	1	7.06	2	31.23	3	68.86	4	120.17	5	185.63	6	265.02	7	358.59	8	466.51
50	1	1.14	2	6.25	3	13.77	4	24.06	5	37.13	6	53.01	7	71.72	8	93.31
100	1	0.71	2	3.12	3	6.89	4	12.03	5	18.57	6	26.51	7	35.87	8	46.66
200	1	0.35	2	1.56	3	3.45	4	6.02	5	9.29	6	13.26	7	17.94	8	23.33
300	1	0.24	2	1.04	3	2.30	4	4.01	5	6.19	6	8.84	7	11.96	8	15.56
400	1	3.21	2	16.31	3	40.81	4	86.53	5	142.38	6	203.66	7	286.03	8	344.15
500	1	2.76	2	14.07	3	34.21	4	71.83	5	123.18	6	174.61	7	250.51	8	299.19
750	1	2.02	2	10.13	3	24.63	4	52.61	5	94.91	6	132.77	7	201.14	8	236.82
1000	1	1.60	2	8.00	3	19.53	4	42.49	5	79.26	6	109.51	7	172.00	8	204.10
1250	1	1.35	2	6.72	3	16.58	4	36.34	5	69.42	6	95.39	7	154.12	8	181.08
1500	1	1.17	2	5.83	3	14.57	4	31.99	5	62.43	6	85.94	7	140.84	8	165.95
1750	1	1.05	2	5.14	3	13.16	4	28.70	5	57.49	6	78.85	7	132.46	8	155.27
2000	1	0.96	2	4.62	3	11.97	4	26.27	5	53.51	6	73.15	7	124.94	8	146.40

Table C.6: 200 kHz inductance values for a thickness from 10 to 2000 μm, for all number of turns with a spacing of 500μm on a 12.5 cm cell. The 2D model is used for a thickness up to 300 μm, after which the 3D model is used.

t (μm)	**N**	**L** (μH)	**N**	**L** (μH)	**N**	**L** (μH)	**N**	**L** (μH)	**N**	**L** (μH)	**N**	**L** (μH)	**N**	**L** (μH)	**N**	**L** (μH)
10	1	0.056	2	0.236	3	0.523	4	0.916	5	1.414	6	2.017	7	2.725	8	3.537
50	1	0.056	2	0.236	3	0.523	4	0.916	5	1.414	6	2.017	7	2.725	8	3.537
100	1	0.056	2	0.236	3	0.523	4	0.916	5	1.414	6	2.017	7	2.725	8	3.537
200	1	0.056	2	0.236	3	0.523	4	0.916	5	1.414	6	2.017	7	2.725	8	3.537
300	1	0.056	2	0.236	3	0.523	4	0.916	5	1.414	6	2.017	7	2.725	8	3.537
400	1	0.016	2	0.073	3	0.209	4	0.419	5	0.790	6	1.168	7	1.782	8	2.387
500	1	0.015	2	0.070	3	0.203	4	0.410	5	0.767	6	1.137	7	1.736	8	2.332
750	1	0.014	2	0.066	3	0.193	4	0.389	5	0.722	6	1.078	7	1.642	8	2.220
1000	1	0.013	2	0.062	3	0.185	4	0.370	5	0.688	6	1.032	7	1.571	8	2.126
1250	1	0.012	2	0.060	3	0.176	4	0.354	5	0.658	6	0.992	7	1.509	8	2.051
1500	1	0.011	2	0.057	3	0.168	4	0.341	5	0.632	6	0.953	7	1.455	8	1.981
1750	1	0.011	2	0.055	3	0.161	4	0.328	5	0.608	6	0.919	7	1.400	8	1.913
2000	1	0.010	2	0.053	3	0.155	4	0.316	5	0.586	6	0.888	7	1.353	8	1.854

D
Current density

(a) 200 μm at 1 Hz

(b) 1000 μm at 1 Hz

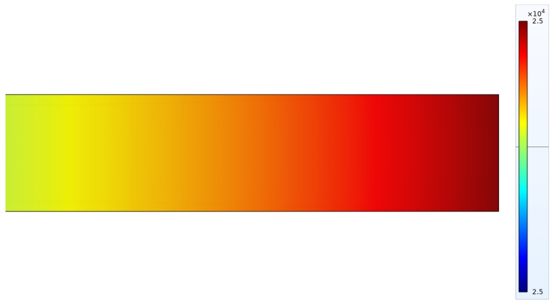

(c) 200 μm at 100 kHz

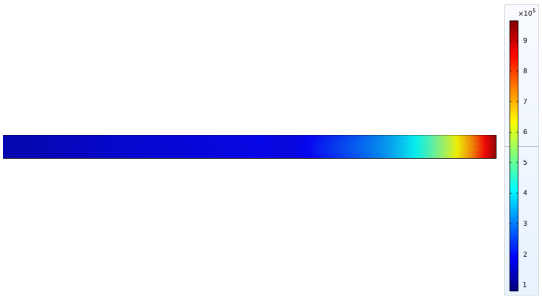

(d) 1000 μm at 100 kHz

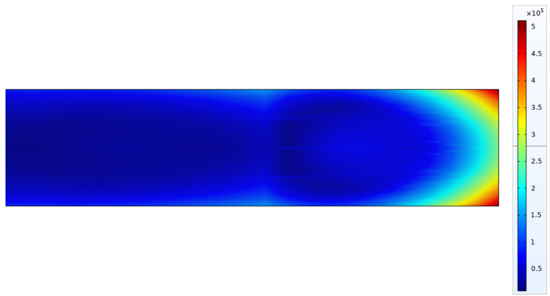

(e) 200 μm at 200 kHz

(f) 1000 μm at 200 kHz

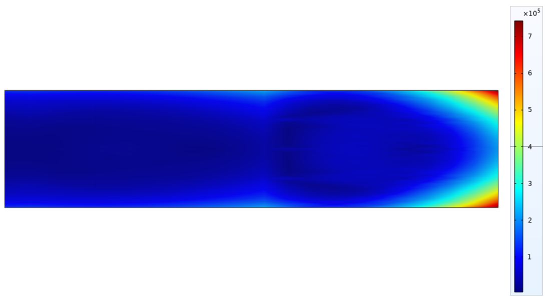

Figure D.1: Current density figures of the 3D straight wire for a thickness of 200 μm on the left (*(a), (c), (e)*) and 1000 μm on the right (*(b), (d), (f)*). The color legend shows the normalized current density in A/m^2 where the first row is for a 1Hz system, the second row a frequency of 100 kHz, and the third row a frequency of 200 kHz.

E

Quality factor

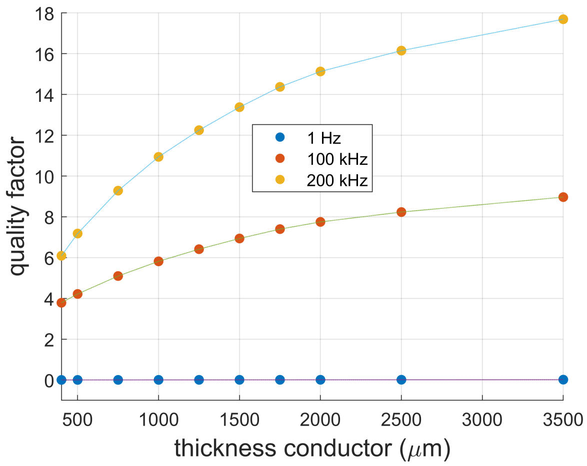

(a) 4 turns

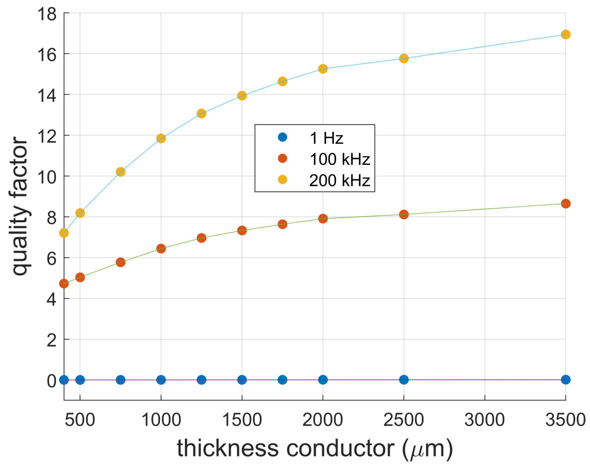

(b) 6 turns

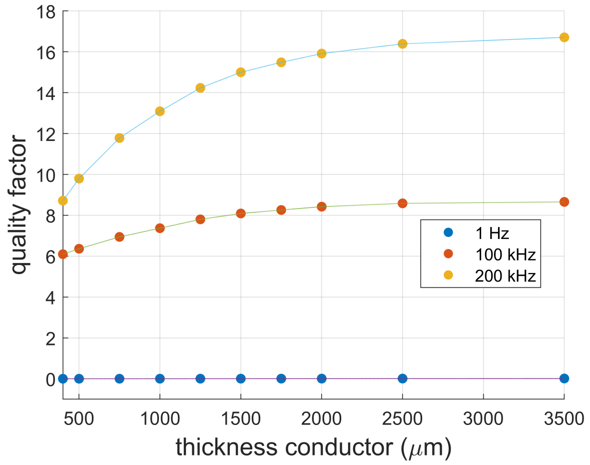

(b) 8 turns

Figure E.1: Quality factor versus conductor thickness for (a) 4, (b) 6, and (c) 8-turn coils.